The Growth of Novel Thin Film Oxides

Calibrations, Preliminary Growths and Quantitative Characterizations

by

Ryan Christopher Wicks

B.Sc., Queen's University, 2005

A THESIS SUBMITTED IN PARTIAL FULFILMENT OF
THE REQUIREMENTS FOR THE DEGREE OF

Master of Science

in

The Faculty of Graduate Studies

(Physics and Astronomy)

The University Of British Columbia

October, 2007

Abstract

In this thesis, preliminary growths of $SrCuO_2$ epitaxial films were under-taken. Despite none of the growths yielding the desired stoichiometry or oxidation, the difficulties that were encountered, such as properly oxidiz-ing the film, are demonstrated to be surmountable. The structure of the films was probed with RHEED, and found to display growth patterns that are consistent with epitaxial growth. The desire to perform future ARPES studies on this material imposes strict sample quality requirements and the need for the most accurate measurements of stoichiometry possible. This warranted an investigation of the properties of the SPECS PHOIBOS 150 hemispherical electron analyzer used to perform XPS measurements of films chemistry. The degree of non-linearity of the electron detection system was determined and a method introduced that could correct for it. Correcting for the transmission function of the analyzer was found to be a necessary step in quantitative chemical analysis. Therefore, transmission functions were mea-sured using two techniques and were found to be in good agreement with calculated transmission functions provided by SPECS. While correcting for detector non-linearity and measuring the actual transmission function did not drastically alter the stoichiometry measurements for scans taken using reasonable analyzer settings for XPS (1% for the films grown in this thesis, mostly from detector non-linearity), it is possible to drive the analyzer into regimes where the corrections will be necessary. The methods used to first correct for the intensity response of the analyzer, and then the transmission function would be more applicable in these instances. The work performed in this thesis will ensure that future growths of $SrCuO_2$ films will yield samples of adequate quality to perform an ARPES study.

Table of Contents

Appendices

List of Tables

List of Figures

List of Abbreviations

AO - Atomic Oxygen

ARPES - Angle Resolved Photo-emission Spectroscopy

CAE - Constant Analyzer Energy (also FAT)

CCD - Charge Coupled Detector

CRR - Constant Retard Ratio (also FRR)

FAT - Fixed Analyzer Transmission

FRR - Fixed Retard Ratio

LEED - Low Energy Electron Diffraction

MBE - Molecular Beam Epitaxy

MCP - Multi-Channel Plate

PLD - Pulsed Laser Deposition

PVD - Physical Vapour Deposition

QCM - Quartz Crystal Monitor

RF - Radio Frequency

RHEED - Reflection High Energy Electron Diffraction

SCCM - Standard Cubic Centimeters per Minute

STM - Scanning Tunneling Microscopy

TMO - Transition Metal Oxide

XPS - X-Ray Photoelectron Spectroscopy

Acknowledgements

I would like to acknowledge the support of *both* my supervisors, Dr. Andrea Damascelli and Dr. Nicholas Ingle. They have both spent considerable time and effort to take me from an ignorant student fresh out of undergrad, to a full-fledged graduate student, just as ignorant, but better able to answer his own questions. Despite each of them having a different perspective and approach to doing science, I know I am a better scientist for having the opportunity to work with both of them.

I would also like to thank the other students and post-docs who worked in the lab with me. You are a valuable source of information and assistance, but, more importantly, you can appreciate a dirty joke, and have made coming to the lab each day interesting.

For my parents, who got me here, and for Marja, who still loves me despite me being me (See figure 1).

Removed Pending Copyright Permission

Figure 1: A graduate student in thesis writing mode.

Chapter 1

Introduction

1.1 Motivation

The transition metal oxides (TMOs) are a strange class of materials. They exhibit a broad spectrum of unique and inexplicable properties, such as colossal magneto-resistance and high temperature superconductivity. The failure of conventional condensed matter physics to explain even the most basic properties of the TMOs' is due to the localized and strongly correlated nature of their outermost electrons. The strong localization of electrons lies at the root of the TMOs more exotic properties. As science begins to obtain a better understanding of the nature of electron correlations in condensed matter systems, new vistas in device fabrication will be revealed, ushering in an era where the striking and bizarre properties of strongly correlated systems, like the TMOs, can be tailored to suit the needs of human ingenuity.

TMOs are characterized by strongly localized electronic orbitals. In a noble metal or semi-conductor, the outermost electrons are of primarily s and p character. The large spatial extent of these orbitals means that the electron density is spread roughly evenly throughout the solid. The interactions between electrons in this approximately homogeneous electron gas are well described by a non-interacting, single particle picture (specifically through the local density approximation of density functional theory). The TMOs, on the other hand, have outermost electrons that consist of d orbitals which are strongly localized. The electron density is no longer homogeneous in these systems, and the electronic correlations cannot be described by the local density approximation. In principle, electrons on one site can tunnel to adjacent sites, but the large electronic density localized at the new site invokes a strong Coulomb repulsion (called U) that prevents this. Systems with half filled orbitals which would normally be metals can behave as insulators with gaps as large as 5-10 eV (Mott-Hubbard insulators, in this case). Strong localization also makes possible various exchange interactions between sites, leading to magnetism in these systems. The host of exciting properties that are displayed by these strongly localized, highly correlated systems make them interesting both from a scientific and technological point

of view.

In an attempt to understand these types of materials, theoretical approaches have been developed that go beyond the local density approximation picture. Tools developed in the field of particle physics to deal with many body interactions have also been adapted for use in condensed matter systems with some success. Overall, however, our understanding of electronic correlations is still incomplete. Fortunately, there are a large number of experimental probes that can be used further our understanding of electronic correlations in solids, and TMOs in particular; for example, Angle Resolved Photo-Emission Spectroscopy (ARPES) or Scanning Tunneling Microscopy (STM). Unfortunately, surface sensitive techniques, such as these, require the use of atomically flat and clean samples to extract meaningful data. This limits the number of systems available for study to those with a natural cleavage plane (a 2-D layer of the crystal that has a weaker bond than adjacent layers, which will break preferentially when subject to mechanical stress).

A heuristic approach to studying these materials would be to modify a parameter of the system and then measure how its properties change. The most common example is chemical doping. Other options could include changing the lattice parameter of the system, or the bond angles between atoms. In a de-localized system, these changes would only have small effects on the overall properties because the electronic densities remain almost unchanged. In a system with localized electrons however, changing the overlap between adjacent orbitals could have enormous effects. Unfortunately, changing lattice parameters and bond angles independent of chemical doping is a difficult challenge in conventional crystal growth, where thermodynamics puts tight constraints on how the material grows.

An alternate approach to modifying a system's parameters uses an alternate method of crystal growth called epitaxy. The goal of epitaxial growth is to form a thin film of single crystalline material through some deposition process on a suitable single crystal substrate. There are two main advantages to epitaxial growth. One advantage of an epitaxial growth technique is that a flat surface, suitable for surface sensitive experiments, is left after growth. The second advantage is that changing the seed substrate changes the potential that the film feels as it forms, creating thermodynamically accessible meta-stable phases that would be otherwise untenable. Epitaxial films are characterized by a shared unit cell at the interface [1, 2]: the substrate and film are "lattice matched" at their common interface. In homo-epitaxy (where the film and substrate are made of the same material) this is not surprising. This behavior in hetero-epitaxy (epitaxy between two different

materials), on the other hand, offers a variety of interesting possibilities for crystal growth. For example, materials normally grown at high pressures by conventional means can be grown epitaxially in a vacuum environment; the potential of the seed substrate provides the needed strain [3]. Hetero-epitaxy can also cause a film to grow with a modified structure, such as altered lattice parameters or bond angles [4]. Furthermore, this structural modification can be achieved without resorting to chemical doping.
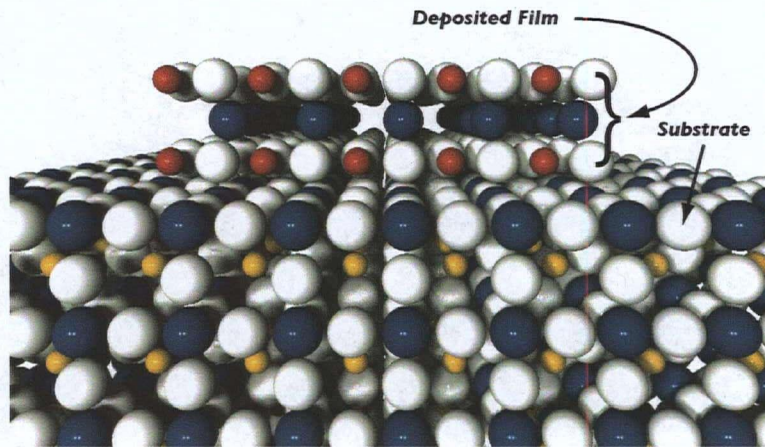
Figure 1.1: A pictorial demonstration of epitaxy (courtesy of Nicholas J.C. Ingle).

The growth of lattice matched films does present its own set of draw-backs. Growth of a strained film promotes the formation of defects in an attempt to relax the film to its thermodynamically stable state. It has been demonstrated, however, that strained TMO films can be grown well past the point where conventional energy and strain considerations predict that they would form defects and relax [3, 5].

Hetero-epitaxy also offers other exciting prospects for engineering the properties of TMOs. If the chosen substrate has a polar unit cell, as many TMO substrates do, the need to balance this polarity leads to many novel possibilities for altering the film's behaviour. Semi-conductors will normally compensate for this "polar catastrophe" by allowing defects and changes in stoichiometry and/or structure at the interface (structural or chemical

reconstruction)[6]. In some systems, however, it is energetically favourable to change the oxidation level of the film's constituents at the interface to compensate for the polar nature of the film rather than to adjust its structure or chemistry [7]. This is called an "electronic reconstruction".
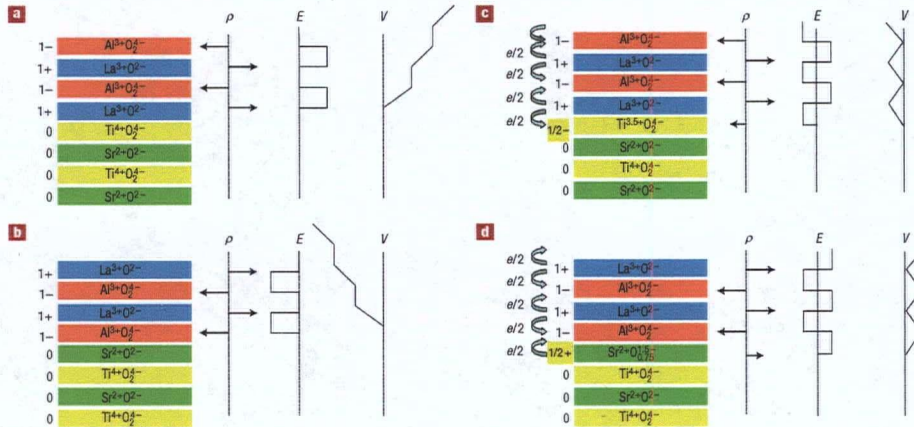
Figure 1.2: The Polar Catastrophe and Electronic Reconstruction. This figure shows the different possible arrangements at the interface between films of $SrTiO_3$ and $LaAlO_3$ (which has a polar unit cell). Parts a and b demonstrate the two ways in which these films can stack, and the resultant divergence of potential with film thickness (the so called "polar catastrophe"). Parts c and d show how this divergence can be avoided by allowing oxidation state of half of the Ti^{4+} to change to Ti^{3+} (an overall change to $Ti^{3.5+}$). In this case, the polar catastrophe is avoided, and the half of an electron per unit cell that is moved to the interface results in a metallic layer between the two insulators. From [8]

This aspect of oxide thin film research has already begun to realize its promise, with the first exciting results of Hwang and coworkers discovering a metallic layer between two insulating oxides ($SrTiO_3$ and $LaTiO_3$) [9] spurring a flurry of related activity. Figure 1.2 provides an explanation of how the interface between insulators can form a metallic layer through an electronic reconstruction. Superconductivity at this interface has also been demonstrated [10]. In the case of cuprate based films, this could be an interesting mechanism for doping the CuO planes deemed essential for high temperature superconductivity without changing the film's stoichiometry (the cuprates are 2-D materials that contain corner sharing CuO planes, and

are the only materials that exhibit high temperature superconductivity).

The potential of using epitaxial growth techniques on TMOs is enormous. There is the obvious advantage of being able to prepare materials with an atomically flat surface, making a wider variety of materials available for surface sensitive measurements. It must be remembered, however, that epitaxy is not only a method for preparing bulk samples suitable for surface science. Ultra-thin films can be distinct materials with properties that are totally unique from their bulk counterparts [11]. The ability to control the structure through the interaction of the substrate on the film could have enormous impact on the electronic properties of the material due to the TMOs strongly localized nature. Electronic reconstructions at the interface between substrate and film also present exciting possibilities for tuning the TMOs properties.

1.2 Scope of Thesis

In this thesis, growth of $SrCuO_2$ is performed on $SrTiO_3$ substrates using Molecular Beam Epitaxy (MBE). $SrCuO_2$ has the simplest structure that still contains the CuO planes considered necessary for high temperature superconductivity. This makes it an interesting candidate for an ARPES study, but this has not happened due to the lack of a cleavage plane in the material. Thin film growth makes this sort of study possible.

To perform a meaningful ARPES study, however, a high sample quality is paramount. Scientific advances in ARPES studies of the TMOs have been more a result of increased sample quality than instrumental resolution. This requires that a careful quantitative chemical analysis of our XPS data is undertaken. As a result, an examination and quantification of the properties of a SPECS PHOBIOS 150 hemispherical electron analyzer is undertaken. The principles of operation and properties of this device will be presented, with an emphasis on the qualities of the analyzer that will be investigated more closely, specifically the transmission function of the analyzer, and the linearity of the detector response with electron intensity. Several methods for determining the transmission function and intensity response of the analyzer will be introduced, and the results of these measurements are discussed.

The results of the chemical analysis reveal that the oxidation level of the $SrCuO_2$ films achieved with the use of molecular Oxygen is insufficient to properly oxidize the $SrCuO_2$ films. As a result, the viability of an alternate Oxygen delivery system is investigated. The effectiveness of a Mantis Deposition MATS 30 RF Atom Source for creating Atomic Oxygen

5

(AO) is determined and compared to other previously characterized AO sources used to grow similar materials epitaxially.

The preliminary growths performed in this thesis are the first steps towards performing a systematic ARPES study of $SrCuO_2$ thin films which before now was impossible due to the inability to cleave the material. This is not only exciting because it offers the chance to study the simplest of the cuprate materials with a surface sensitive measurement technique, but also because epitaxial growth offers a variety of novel mechanisms for altering the electronic structure of the material; through substrate lattice matching to change the lattice parameters and bond angles, or through a substrate/film interaction, such as an electronic reconstruction at the substrate/film interface. The lessons learned through these preliminary growths, and the subsequent analyzer and AO source calibrations ensure that future studies will have the highest chances for success.

Chapter 2

Calibration of an Electron Analyzer

2.1 Introduction

The requirement of samples of high quality in performing future ARPES measurements on $SrCuO_2$ films requires that the stoichiometry and oxidation of the films be known to the highest possible precision. To extract this information from a thin film, the best tool is photo-emission spectroscopy. The details of the technique will be discussed more thoroughly in section 3.2, but at its heart, the measurement involves collecting electrons being excited out of the sample into the vacuum, discriminating them as a function of their kinetic energy, and then recording this spectrum. The tool used to do this is an electron analyzer, and this chapter looks at different techniques for correcting non-linearities in its intensity response and transmission.

2.1.1 The Electron Analyzer

The function of an electron analyzer is to measure the kinetic energy distribution of collected charged particles. This ability has made them a very popular and versatile tool for both research and industry. There are several companies offering commercial analyzers. There have been many different designs, but the most common design is the electrostatic hemspherical analyzer. For a description of other analyzer designs, please see reference [12]. It should be noted that, in principle, any charged particle can be studied; however, in practice, these analyzers are only used in electron spectroscopies. This is primarily due to the low count rates found in experiments that study other types of particles. Most electron analyzers are designed to operate at higher count rates than are found in these types of studies.

Modern hemispherical electron analyzers have two active components (figure 2.1). The first stage is the accelerating/focusing stage. Electrons enter the analyzer through an electron lens system. This stage has the dual task of focusing electrons on the entrance of the hemisphere, as well as

Removed Pending Copyright Permission

Figure 2.1: Components of an Electron Analyzer (Adapted From [13])

accelerating them in preparation for the next stage. Earlier electron analyzers could only accelerate the impinging electrons, preparing them for the second stage energy discrimination. Modern analyzers, with their electron optics, make possible a variety of different types of focusing (which usually require the use of a 2-D detector). In this thesis, a SPECS PHOIBOS 150 hemispherical electron analyzer is used. Some of the modes available on the this analyzer include transmission modes which boost low signals, magnification modes that magnify a part of a sample, and angle resolved modes useful in Angle Resolved Photo-Emission experiments. These modes are detailed in table 2.1. The second component of the electron analyzer is the hemispherical capacitor. The electrons entering between two concentric hemispheres at different voltages follow a curved path from the entrance slit to the detection system due to a Lorenz force acting on the electrons. The detection system can be either a Charge Coupled Detector (CCD) recording a phosphour screen detecting the electrons that have been amplified by a Multi-Channel Plate (MCP) in newer systems, or a set of channeltrons in older or custom designed systems. The range and median kinetic energy of the electrons that are incident on the screen, as well as the resolution of the analyzer are all defined by the "pass energy" of the analyzer.

The concept of a pass energy needs to be defined because the term oc-

8

Mode	Characteristics	Use
Magnification	-spatially resolved studies with non-monochromated x-ray sources -acceptance area defined by lens, not iris	Small Area XPS
Transmission	-spatially resolved studies requiring strong signal -acceptance area defined by iris, not lens	High Energy or Low Intensity XPS
Angular Dispersion	-Fourrier electron optics give angular dependent information -increased angular range limits energy range	Angle Resolved Photoemission Spectroscopy (ARPES)

Table 2.1: The Various Lens Modes of an Electron Analyzer [14]

curs often in discussions of the operation of an electron analyzer. Electrons that enter the center of the hemispherical analyzer with a kinetic energy that equals the "pass energy" of the analyzer will arrive at the center of the detection system. Electrons that enter the system with energies not at the pass energy are deflected by an amount proportional to the difference between their energy and the pass energy. Hence, the hemispherical capacitor acts as an energy discriminator. The window of kinetic energies exposed to the detector is proportional to the pass energy, as is the resolution of the analyzer.

Modes of Operation

The narrow energy window exposed to the detection system at a fixed pass energy is rarely sufficient to perform a proper experiment. Data is normally acquired by scanning the analyzer through a range of kinetic energies. In practice, this is done by changing the voltages on different parts of the electron analyzer so that only electrons with the desired kinetic energy reach the detection system. The energy window exposed to the detection system at different kinetic energies is then averaged to produce the final spectrum. There are two ways of doing this.

The mode used historically in Auger Electron Spectroscopy is the Fixed Retard Ratio mode (FRR mode) or Constant Retard Ratio (CRR mode). In this mode, the accelerating potential in the electron lens system is held constant (the retarding ratio is constant). To measure a range of kinetic

energies, the pass energy of the hemisphere is scanned. Scanning the pass energy of the hemisphere has the additional effect of changing the range of kinetic energies that are exposed to the detection system. The main advantage of this mode is that one has high intensity at large kinetic energies due to a wider energy window in this range; data collected at high kinetic energy has a larger energy window exposed to the detector, and is sampled for longer, resulting in more intense photoelectron peaks. This will be discussed later, in the context of a transmission function in FRR mode that is approximately linear in kinetic energy. The disadvantage of this mode is that the increased energy window that increases the signal also changes the energy resolution (the resolution worsens as kinetic energy increases). FRR mode is the ideal choice for studies that are interested in identifying the position of weak photoelectron peaks at high kinetic energy where resolution is a secondary concern,

In XPS, Fixed Analyzer Transmission mode (FAT mode), or Constant Analyzer Energy mode (CAE mode), is used. In this mode, the hemispheres pass energy is held constant (fixing the analyzers transmission), and the electrons are accelerated to the pass energy by the lens system. Now, the energy window exposed to the detector remains a constant width as the kinetic energy is scanned. The advantage of this approach is that the instrumental resolution, which is proportional to the pass energy, remains constant over the entire kinetic energy range. The primary disadvantage is a lowering of intensity at high kinetic energies relative to a spectra obtained in FRR mode (see figure 2.2). FAT mode is used when a quantitative analysis of peak shape and size is required.

The Transmission Function

In addition to the two primary modes of operation, there are many other settings that can be changed on modern spectrometers. In the case of the SPECS PHOBIOS analyzer, an iris, as well as entrance and exit slits change the acceptance area or the acceptance angle of the analyzer. Different combinations of voltages in the lens also provide different types of focusing of the electrons entering the analyzer (these are the lens modes, see table 2.1). Changing any of these settings also changes the intensity of the final spectrum. The function that describes these changes is called the transmission function.

The transmission function describes the ability of the electron analyzer to allow electrons to pass through it. Ideally, the analyzer would have no impact on the signal it was measuring. In reality, the analyzer has a significant effect
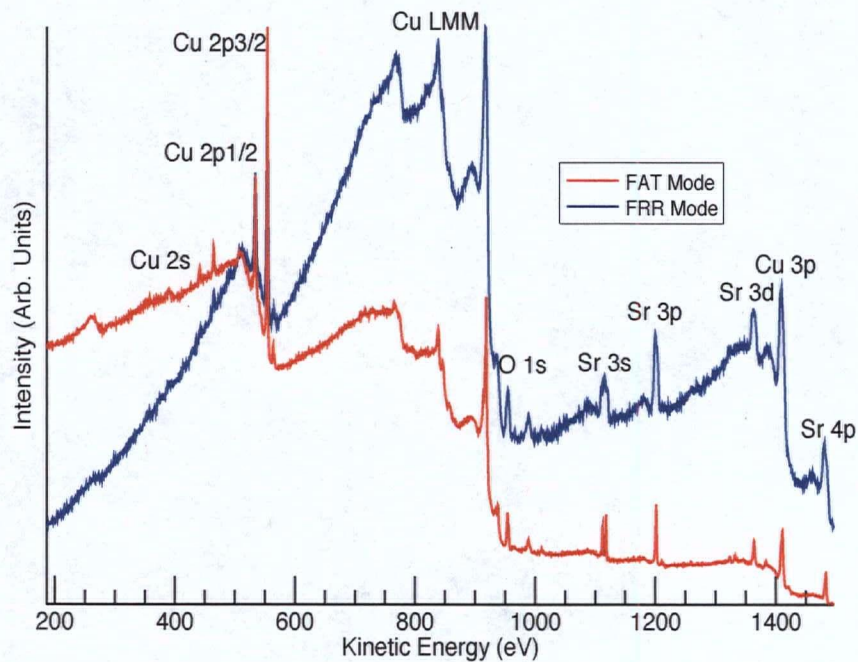
Figure 2.2: XPS scans of the same $SrCuO_2$ sample in FAT and FRR modes. Notice that in FRR mode the intensity of the signal increases as the kinetic energy increases. This highlights the importance of understanding the behaviour of the transmission function in different analyzer modes when performing quantitative peak analysis. Also notice how the width of the peaks in FRR mode increase as the kinetic energy increases (relative to the FAT mode peaks).

on the measured signal (see figure 2.2). The transmission function describes how the intensity depends on the kinetic energy being measured; if one wants to make a quantitative measurement of intensity, it has to be corrected for.

The transmission function of an electron analyzer is rarely taken into account properly when performing experiments. Approximate theoretical transmission function corrections are applied to the data, or tabulated, analyzer specific structure factors are used (see section 3.2.2). This is primarily due to the fact that measuring a transmission function exactly is a difficult task. In this thesis, two separate methods for determining the transmission function are investigated.

Linearity of Detector Response

The transmission function describes the kinetic energy dependent intensity response of the analyzer. There is another effect that alters the measured signal: the intensity response of the detection system. Ideally, the flux measured by the detection system is proportional to the flux incident on the detection system. In reality, at large count rates, the system saturates and no longer responds linearly with applied flux (see figure 2.3). This high intensity behaviour is undesirable, but expected. Most measurement systems have a dead time, the time after a measurement during which the detector cannot respond to new events. At low flux, the period between events is much longer than the dead time of the detector, and all of the events are recorded. At high flux, however, the period between events approaches the dead time, creating the possibility that a measurement event occurs during the dead time and is not recorded. As the incident flux continues to increase, the detector approaches the saturation limit, where the measured rate is equal to the inverse of the dead time. In this limit the detector is useless. A common but limiting method for avoiding this problem is to simply ensure that the detector is always operated in the low count, linear range. A better way would be to measure, and then correct for, the intensity response of the detection system, making available a much larger range of detection. Not only does this increase the dynamic range of the detection system, but it has been previously demonstrated that the response of the detection system commonly used in new electronic analyzers (MCP/phosphour screen/CCD detection system) has a low intensity quadratic response to applied flux [15]. This surprising result indicates that limiting the range of intensities is an inadequate method of dealing with the linearity of the detector, and that measuring the intensity response is a necessary calibration step for performing quantitative photoelectron spectroscopy.
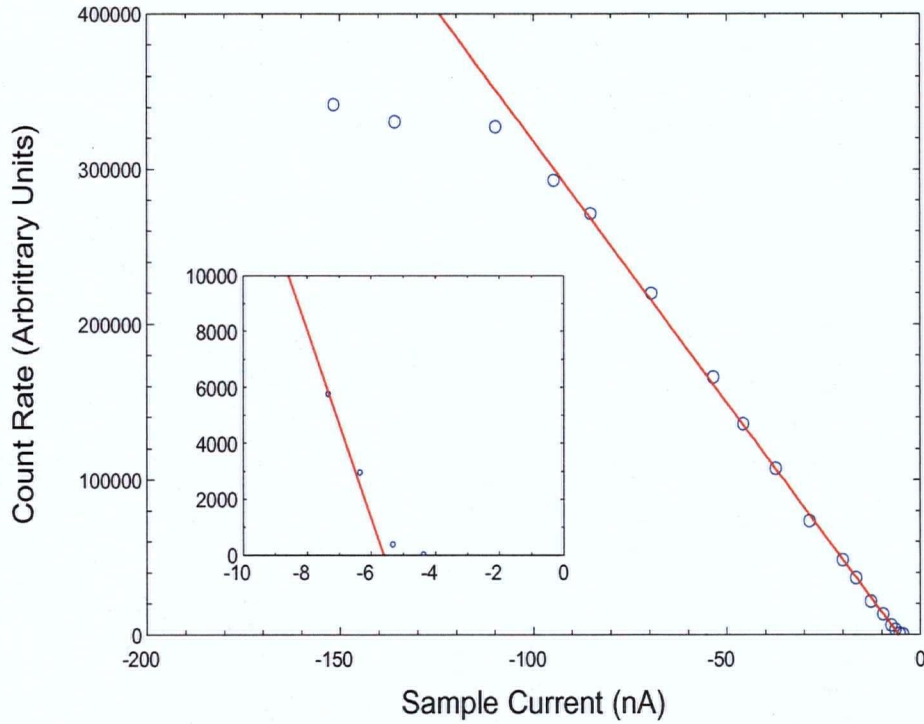
Figure 2.3: Intensity response of the SPECS Phobios detection system (a MCP/phosphour screen/CCD based system). The system responds linearly over a large region. The saturation of the detector can be seen at high intensities. A small quadratic response is evident at low intensities (inset) (From [16]).

2.2   Experiment and Results

2.2.1   Intensity Calibration

Correcting for the detection systems non-linearities must be done before calculating the transmission function. The method used in this thesis to correct for non-linearities in the detection system is based on the one used in reference [15]. This method involves taking several scans of the same sample at different X-ray powers. Scans of the same sample taken at N different x-ray powers yields broad range of intensities at all sampled kinetic energies. The premise of the method is that the real intensity can be represented as a linear combination of the measured intensity raised to different exponents (up to a maximum exponent of P, chosen as the lowest exponent that gives a reasonable fit)(equation 2.1).

$$r(n_j, E_k) \;=\; \sum_{i=0}^{P} a_i \times (m(n_j, E_k))^i \tag{2.1}$$

$r(n_j, E_k)$ is the real spectrum, corrected for detector non-linearities, as a function of kinetic energy E_k and x-ray power n_j, while $m(n_j, E_k)$ is the uncorrected, measured spectrum. The spectra each contain Q equally spaced kinetic energy values. The initial co-effiecient, a_0 is the dark count value, or the value that all the scans approach as the x-ray power goes to 0. As all of the spectra are of the same sample in the same position, and have the same analyzer settings, the real spectra normalized by current should all be equivalent. Substituting equation 2.1 into equation 2.2 yields equation 2.3.

$$\frac{r(n_j, E_k)}{n_j} \;=\; \frac{r(n_1, E_k)}{n_1} \tag{2.2}$$

$$\frac{1}{n_j} \sum_{i=0}^{P} a_i \times (m(n_j, E_k))^i \;=\; \frac{1}{n_1} \sum_{i=0}^{P} a_i \times (m(n_1, E_k))^i \tag{2.3}$$

j labels scans between 2 and N. Scan 1 is chosen to be in the linear range of the detector, as all of the other scans will be corrected relative to it. The choice of an appropriate scan 1 is the most subjective part of the process as it is based entirely on the users experience with the analyzer, and can also introduce an unavoidable systematic error because of the wide range of intensities in a single spectra.

Arbitrarily setting $a_1 = 1$ (this is an algebraic convenience, and allowed because real and measured count rates are allowed to different by an arbitrary factor) and rearranging equation 2.3 gives:

$$\frac{m(n_j, E_k)}{n_j} - \frac{m(n_1, E_k)}{n_1} = a_0 \times \left(\frac{1}{n_1} - \frac{1}{n_j} \right) +$$

$$\sum_{i=2}^{P} a_i \times \left(\frac{(m(n_1, E_k))^i}{n_1} - \frac{(m(n_j, E_k))^i}{n_j} \right) \quad (2.4)$$

This can be re-written as a matrix equation via the following definitions:

$$\mathbf{A} = \begin{bmatrix} a_0 \\ a_2 \\ a_3 \\ \vdots \\ a_P \end{bmatrix} \quad (2.5)$$

$$\mathbf{B} = \begin{bmatrix} m_{2k_1} - m_{1k_1} \\ m_{2k_2} - m_{1k_2} \\ \vdots \\ m_{2k_Q} - m_{1k_Q} \\ m_{3k_1} - m_{1k_1} \\ m_{3k_2} - m_{1k_2} \\ \vdots \\ m_{3k_Q} - m_{1k_Q} \\ \vdots \\ \vdots \\ m_{Nk_1} - m_{1k_1} \\ m_{Nk_2} - m_{1k_2} \\ \vdots \\ m_{Nk_Q} - m_{1k_Q} \end{bmatrix} \quad (2.6)$$

$$\mathbf{C} = \begin{bmatrix} \frac{1}{n_1} - \frac{1}{n_2} & \frac{(m_{1k_1})^2}{n_1} - \frac{(m_{2k_1})^2}{n_2} & \frac{(m_{1k_1})^3}{n_1} - \frac{(m_{2k_1})^3}{n_2} & \cdots & \frac{(m_{1k_1})^P}{n_1} - \frac{(m_{2k_1})^P}{n_2} \\ \frac{1}{n_1} - \frac{1}{n_2} & \frac{(m_{1k_2})^2}{n_1} - \frac{(m_{2k_2})^2}{n_2} & \frac{(m_{1k_2})^3}{n_1} - \frac{(m_{2k_2})^3}{n_2} & \cdots & \frac{(m_{1k_2})^P}{n_1} - \frac{(m_{2k_2})^P}{n_2} \\ \vdots & \vdots & \vdots & \ddots & \vdots \\ \frac{1}{n_1} - \frac{1}{n_N} & \frac{(m_{1k_Q})^2}{n_1} - \frac{(m_{Nk_Q})^2}{n_N} & \frac{(m_{1k_Q})^3}{n_1} - \frac{(m_{Nk_Q})^3}{n_N} & \cdots & \frac{(m_{1k_Q})^P}{n_1} - \frac{(m_{Nk_Q})^P}{n_N} \end{bmatrix} \quad (2.7)$$

$$\mathbf{B} - \mathbf{CA} \;=\; 0 \tag{2.8}$$

$\mathbf{A}$ is a column vector of length P, $\mathbf{B}$ is a column vector of length $(N - 1) \times Q$ and $\mathbf{C}$ is a $(N - 1) \times Q$ by P matrix. m_{ik_j} is the j'th kinetic energy point of the i'th dataset. j goes from 1 to Q, the length of each spectrum, and i goes from 2 to N, the number of spectra. Equation 2.8 is equivalent to equation 2.4. Simply solving for $\mathbf{A}$ will not yield the coefficients because of statistical errors found in real data. The best that can be done is to find the most likely values by minimizing $|\mathbf{B} - \mathbf{CA}|^2$ (solving the normal equation).

$$\nabla_A |\mathbf{B} - \mathbf{CA}|^2 \;=\; 0 \tag{2.9}$$
$$2\mathbf{C}^T\mathbf{CA} - 2\mathbf{C}^T\mathbf{B} \;=\; 0 \tag{2.10}$$
$$\mathbf{A} \;=\; \left(\mathbf{C}^T\mathbf{C}\right)^{-1} \times \mathbf{C}^T\mathbf{B} \tag{2.11}$$

Solving equation 2.11 will yield the coefficients needed to express the true intensity in terms of the measured intensity. The values can be substituted into equation 2.1 and applied to any other scan as long as the intensity values are within the range that was used in the calibration. The algorithm used for finding the coefficients and correcting the data are provided in Appendix A.

This algorithm was successfully applied to a set of seven Copper scans taken in Medium Magnification mode. A section of the data around the Cu $2p$ peaks after normalization by x-ray power but before intensity correction is shown in figure 2.4. While the different datasets are similar, there is a definite difference in the various intensities. The inset shows the normalized intensity of the $2p_{\frac{3}{2}}$ peak. Ideally, the data would be a flat line. This data does display a trend that suggests that the detection system is being operated in both the saturation and low intensity regimes, as well still having a multiplicative scaling factor missing. To claim this with certainty, however, the true current of electrons being photo-emitted from the sample should be measured directly, rather than inferred through an indirect measurement of X-ray power.

The algorithm was applied to correct the data to various powers. A plot of the data corrected with a $P = 6$ exponent is shown in figure 2.5. Higher order than $P = 6$ does not significantly improve the quality of the correction. A mode or measurement yielding higher intensities and hence stronger non-linearities would be expected to require higher order corrections. The data in figure 2.5 now appear to be properly normalized because the different datasets now lie on top of each other, and the intensity of the $2p_{\frac{3}{2}}$ peak as a

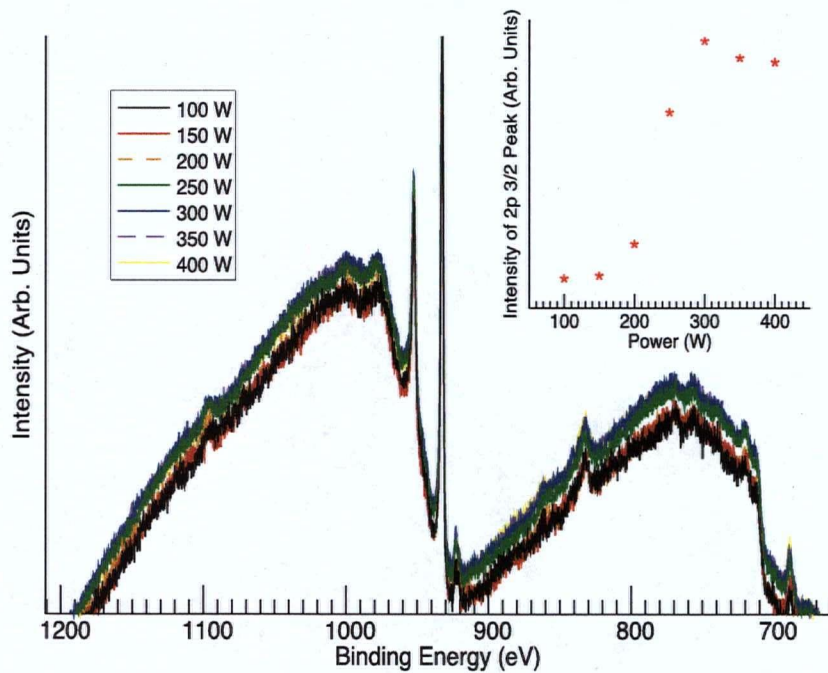Figure 2.4: A portion of a Cu spectrum, normalized for X-ray power, but not intensity corrected. The inset shows the peak area intensity of the Cu $2p_{\frac{3}{2}}$ peak. The intensity appears to display non-linearity, saturating at high X-ray powers, and also appears to display quadratic behaviour at low intensities. There is also a multiplicative constant that was not accounted for in the normalization.

function of X-ray power is flat. This indicates that the non-linearities have been corrected.
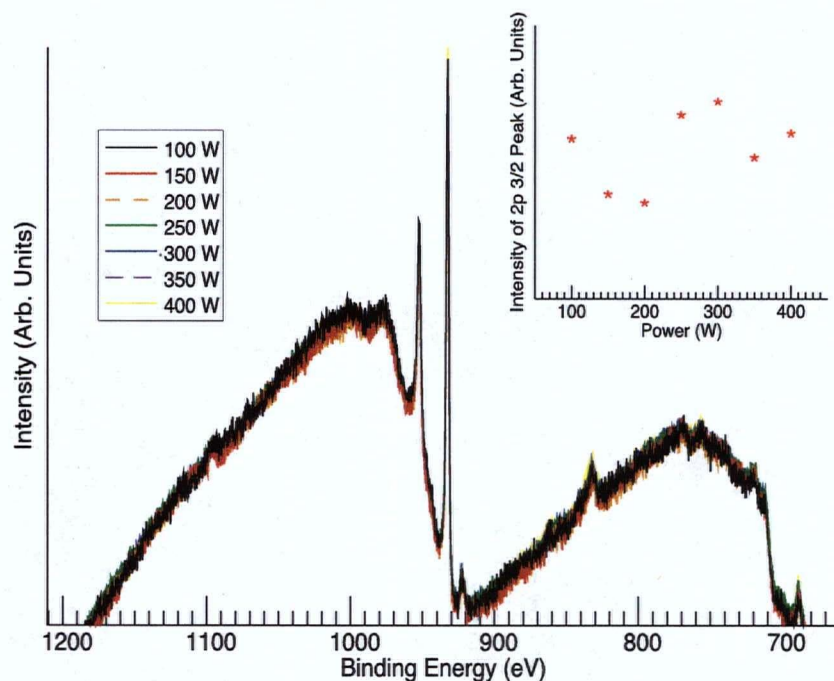
Figure 2.5: A portion of a Cu spectrum.that has been normalized for X-Ray power and intensity corrected. This is a considerable improvement over the uncorrected data shown in figure 2.4. The non-linear behaviours appears to have been corrected by the algorithm with a maximum exponent of $P = 6$. The range of intensities of the inset is same as the inset of figure 2.4.

In figure 2.6, the measured intensity is plotted as a function of the actual (corrected) intensity. This plot bears many similarities to the data provided by SPECS regarding the intensity response of the detection system (figure 2.3). The detector is beginning to saturate at high intensities, and displays quadratic behaviour at low intensities. The saturation at high intensities is by far the most pronounced, but only the most intense peaks were affected. However, the settings used to collect this data were probably conservative in terms of maximum intensities for an average XPS measurement. Therefore, correcting these non-linearities is an important step in performing any quan-

18

titative analysis of data collected by this electron analyzer. This includes calculating transmission functions, as well as performing quantitative chemical analysis. In the case of the $SrCuO_2$ films grown in this thesis (discussed in the next chapter), correcting for the intensity accounted for an approximately 1% difference in the measurement of stoichiometry.
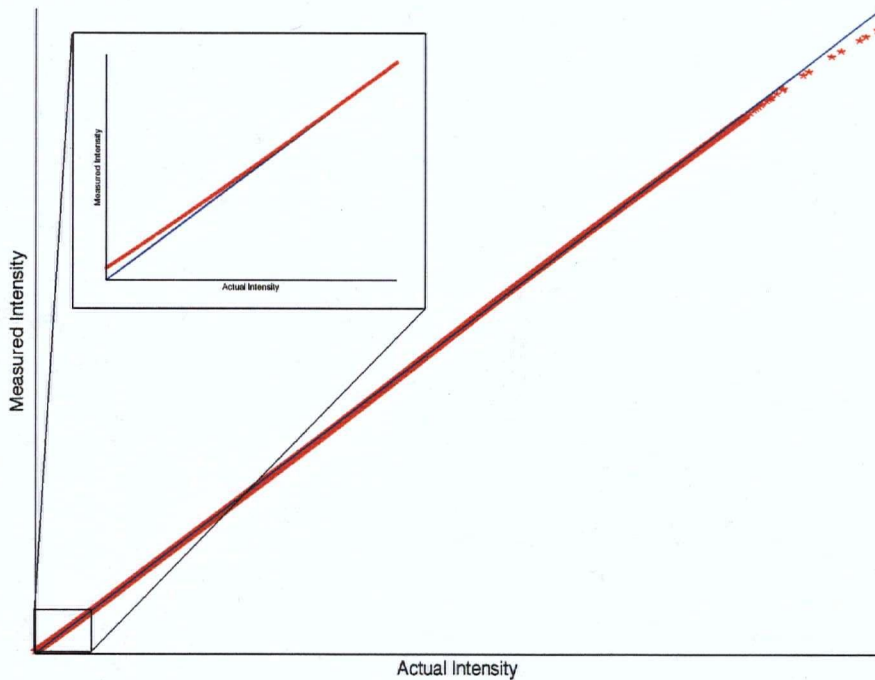
Figure 2.6: Measured intensity response of the SPECS PHOIBOS detection system. The measured intensity is plotted as a function of the actual (corrected) intensity. The blue line represents linear behavior. At high count rate, the detector begins to saturate, and at low count rates, the detector displays a quadratic response. This agrees qualitatively with the expected analyzer response, as well as the information provided by the manufacturer (see figure 2.3). The data shown in figures 2.4 and 2.5 correspond to the high count rate region of this graph.

2.2.2 The Transmission Function

Once the intensity response has been corrected, it is possible to measure the analyzer's transmission function. If the transmission function for one combination of settings of an analyzer is known, it is trivial to find the transmission function for any other combination of settings experimentally. By measuring a spectra of any sample with the analyzer set to a mode with a known transmission function, and then re-measuring the same sample with only the analyzer settings changed, the unknown transmission function can be extracted.

$$TF_{unknown} = \frac{I_{unknown}}{I_{known}} TF_{known} \qquad (2.12)$$

There have been many different techniques suggested to measure the transmission function of an electron analyzer [17, 18]. Here, two techniques have been used. The first technique, the FAT/FRR ratio, is very simple, but assumes a known transmission function for one mode and a limited functional form for the other. The second technique, the transmission function using peak intensities, is more robust than the first method because it assumes a more flexible functional form for the transmission function without assuming a known transmission function for any mode. Each technique yields a function that is proportional to the transmission function, but since all quantitative XPS measurements yield relative quantities, this is not a problem. Both methods take into account and correct for the additional kinetic energy dependance of the photoelectron cross section, σ, and the mean free path of the photoelectrons, $F(E_k)$.

Method I: FAT/FRR Ratio

The premise of this method is to assume a known form for the FRR mode transmission function (a linear transmission function) and use this to find the transmission function in FAT mode by assuming a functional form for it [19, 20]. The ideal transmission functions for the two modes based on electron optics calculations are:

$$T_{FAT}(E_k) = \frac{PE^2 K}{E_k} \qquad (2.13)$$

$$T_{FRR}(E_k) = \frac{E_k K}{RR^2} \qquad (2.14)$$

E_k is the kinetic energy, PE is the pass energy of the hemisphere (both in units of eV), RR is the retard ratio of the lens and K is an analyzer dependent constant (both dimensionless). If one takes a scan in both FRR and FAT mode of the same sample with the same photon flux, the ratio for an ideal analyzer will have the form

$$R(E_k) = \frac{[(PE)(RR)]^2}{E_k^2} \qquad (2.15)$$

By taking the ratio of measured spectra, all of the terms from equation 3.4 that do not depend on the analyzer mode cancel out. If the analyzer is not ideal, the ratio is modified by assuming that FRR mode retains its linear form, but that FAT mode becomes an inverse function of kinetic energy raised to a variable power, resulting in the following form [20]:

$$R(E_k) = \frac{[(PE)(RR)]^{1+x}}{E_k^{1+x}} \qquad (2.16)$$

Where x is a constant with a value close to 1 (a value of 1 would indicate ideal behaviour). x is found by fitting the measured $R(E_k)$ to equation 2.16. The transmission function in FAT mode is then given by:

$$T_{FAT} \propto \frac{1}{E_k^x} \qquad (2.17)$$

The primary advantage of this method is that it is very easy to implement.

Figure 2.7 shows $R(E_k)$ for settings of medium magnification, iris 23, slits set to 1.6X20 and 2:open, pass energy of 60 eV and a retard ratio of 15.

As seen in figure 2.7, it is not possible to fit the entire range of data with the simple function given by equation 2.16. At high KE, the exponent x is closer to the theoretical value of 2 and the fitted constant is closer to the expected product of the retard ratio and pass energy raised to the exponent $1+x$. At low KE, the function does fit the data well, but the values obtained are not what one would expect. This suggests that the model presented in equation 2.16 is not valid at low kinetic energies. This is supported by the data in figure 2.8.

Figure 2.8 is a plot of the expected and measured product of the pass energy and retard ratio. Fits were done to each 100 eV section of $R(E_k)$
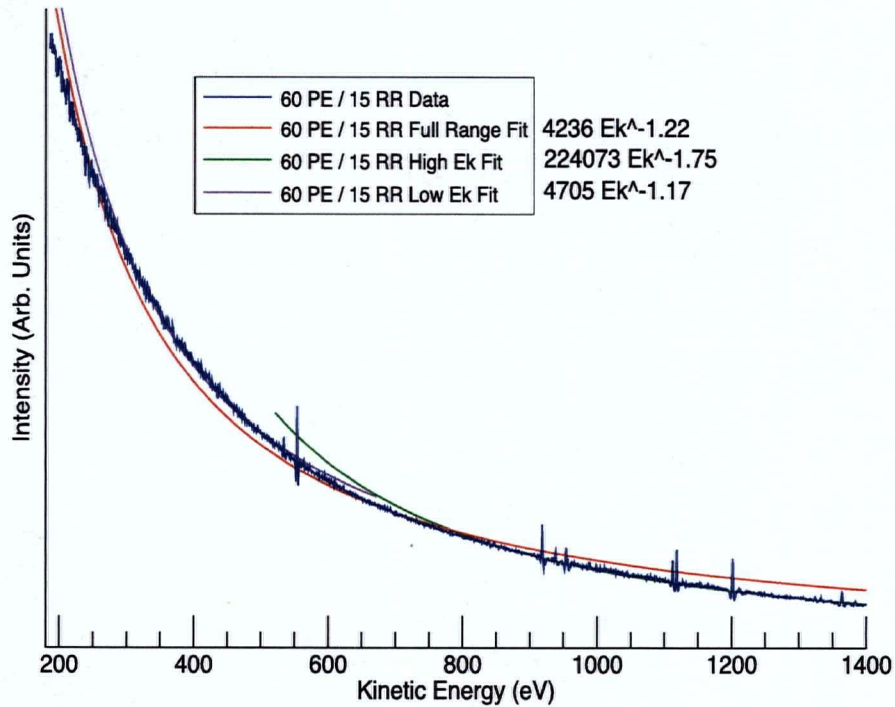
Figure 2.7: Fit to data for Method I. The fit to the full dataset does not match the data well, and the fitted parameters are not what one would expect based on the model in equation 2.16 (the constant does not equal $((PE)(RR))^{1+x}$ and the exponent does not equal 2). At low kinetic energy the fitted values deviate even more strongly from the expected behaviour. At high kinetic energies, however, the fitted values agree well with the expected fit values.
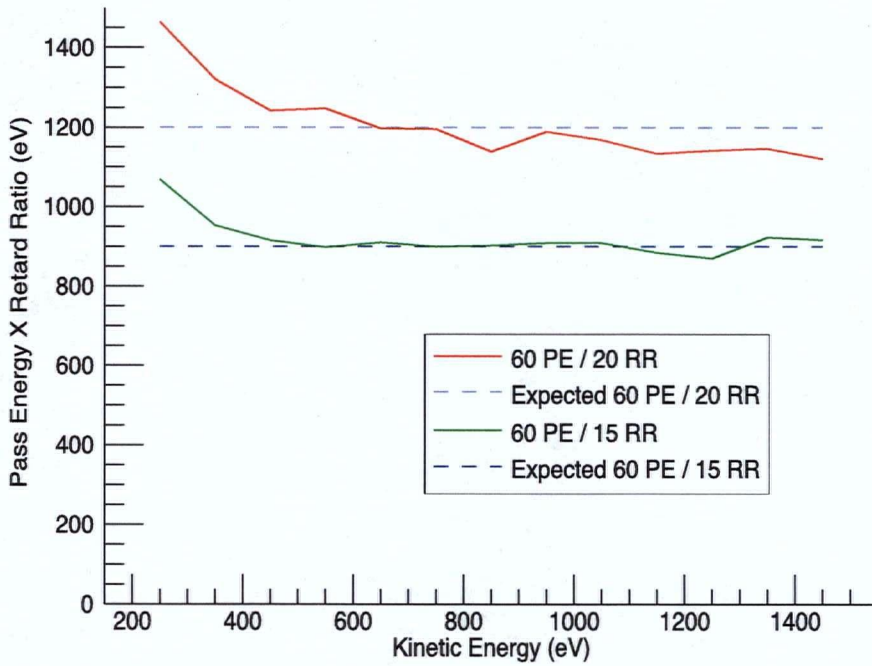
Figure 2.8: Measured and Expected Product of (PE)(RR) for two Different Ratios. The values fit at high kinetic energies agree well with the model function, equation 2.16. At low kinetic energies, however, the fit values begin to deviate from the expected behavior.

for scans with the same settings as figure 2.7. The measured values were obtained from the fitted constant, C, and fitted exponent, $(1+x)$.

$$C = [(PE)(RR)]^{1+x} \qquad (2.18)$$
$$(PE)(RR) = C^{-(1+x)} \qquad (2.19)$$

Figure 2.8 show that at low kinetic energy, the measured constant deviates more strongly from the expected value. This suggests that this method is not effective at low kinetic energies. It is shown in the next section that the reason for this behavior is that the assumption of a linear transmission function in FRR mode is incorrect.

Method II: Transmission Function From Peak Intensities

This method of determining the transmission function assumes a functional form for the transmission function, yet allows enough freedom in the parameters of that model to fit any function [17, 18, 21]. It does not require assuming a known transmission function for any analyzer mode. The functional form of the transmission function chosen for FAT mode is given by equation 2.20

$$T \propto PE \left(\frac{PE}{E_k}\right)^{n\left(\frac{PE}{E_k}\right)} \qquad (2.20)$$

Where n is a function of $\frac{PE}{E_k}$. This is the same functional form as was postulated in method I, but now, instead of a constant exponent x, we have a function $n\left(\frac{PE}{E_k}\right)$. Inserting equation 2.20 into equation 3.4, placing the various constants into the factors A and $B(E_k)$, and taking the natural logarithm of both sides yields:

$$A = xf\phi yA \qquad (2.21)$$
$$B(E_k) = \dot{\sigma}(E_k)F(E_k) \qquad (2.22)$$
$$I = AB(E_k) \left(PE \left(\frac{PE}{E_k}\right)^{n\left(\frac{PE}{E_k}\right)}\right) \qquad (2.23)$$
$$\ln \frac{I}{PE} = \ln A + \ln B(E_k) + n \left(\frac{PE}{E_k}\right) \ln \frac{PE}{E_k} \qquad (2.24)$$

24

One approach to collecting data to find the transmission function is to measure peak areas from XPS scans of the same sample at different pass energies. Alternatively, one can use an electron gun at different kinetic energies. In this thesis, an electron gun was used instead of a XPS scan because it provided more peaks at evenly spaced kinetic energy levels.

$$n \left(\frac{PE}{E_k} \right) = A + \ln \frac{PE}{E_k} B + \left(\ln \frac{PE}{E_k} \right)^2 C \qquad (2.25)$$

The data is shown in figure 2.9 was taken with the same analyzer settings used for correcting the detector non-linearity (Medium Magnification mode, slits set to 1.6:20, 2:open and with an iris of 15), with $\ln \frac{I}{PE}$ plotted as a function of $\ln \frac{PE}{E_k}$. The logarithm of the data must be taken so that when it is plotted, multiplicative factors become constant additive constants ($\ln A$ and $\ln B(E_k)$ from equation 2.20). For each kinetic energy value, the constants can be subtracted off so that data from different kinetic energies can be compared to each other. Finally, the function $n \left(\frac{PE}{E_k} \right)$ (chosen to be a quadratic in this case) can be fitted to the data. See figure 2.10 for the offset corrected and fitted data.

Higher order than quadratic did not significantly improve the fit of n. The resultant FAT mode transmission function agreed well with the calculated function provided by SPECS as shown in figure 2.11. A small deviation is present, but it is still within the spread of the SPECS data. The measured difference in stoichiometry between the measured and calculated transmission function of the $SrCuO_2$ films grown in the next chapter was much less than 1% (not correcting for the transmission function at all, however, introduced a difference of about $2-3\%$).

The calculated and experimental transmission functions were used to calculate the actual transmission function in FRR mode using equation 2.12. The experimentally determined FRR transmission function is shown in figure 2.12. The data does not exhibit the expected linear behaviour. This is most likely the reason for the poor results obtained using Method I. The FRR transmission function found using the calculated data from SPECS deviated from linear behaviour in a similar way.

2.3 Conclusions

A method for correcting the intensity response of the detection system of a SPECS PHOIBOS 150 Hemispherical Analyzer has been investigated.
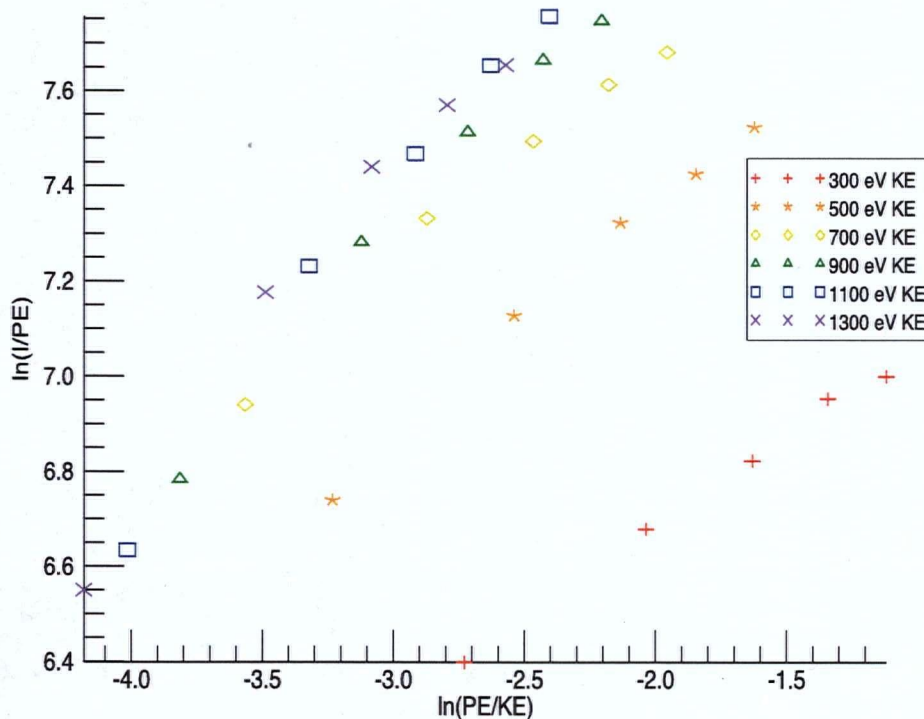
Figure 2.9: $\ln \frac{I}{PE}$ versus $\ln \frac{PE}{E_k}$ for an electron gun. Each point represents the area under the main peak from an electron gun at a fixed current. For each kinetic energy, a scan was taken at different analyzer pass energies. By plotting $\ln \frac{I}{PE}$ versus $\ln \frac{PE}{E_k}$, unknown multiplicative constants can be subtracted off.
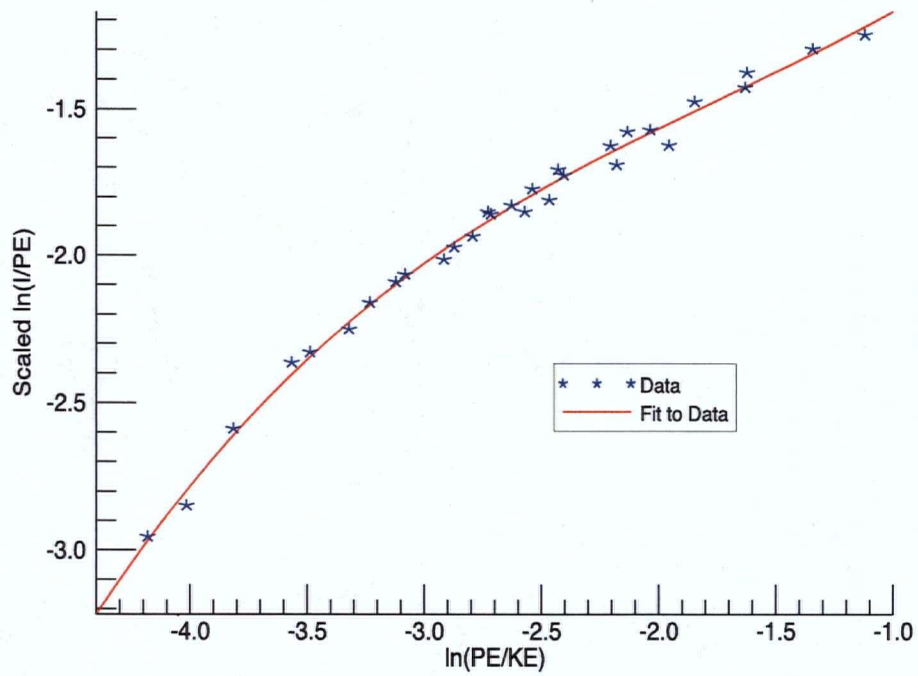
Figure 2.10: Offset corrected and fitted data from the electron gun. This data is the same as shown in figure 2.9, but with the unknown offsets corrected. The fitted n is the unknown transmission function exponent from equation 2.20. It has the form $n\left(\frac{PE}{E_k}\right) = 0.717 + 0.196 \times \ln\left(\frac{PE}{E_k}\right) + 0.038 \times \left(\ln\left(\frac{PE}{E_k}\right)\right)^2$.
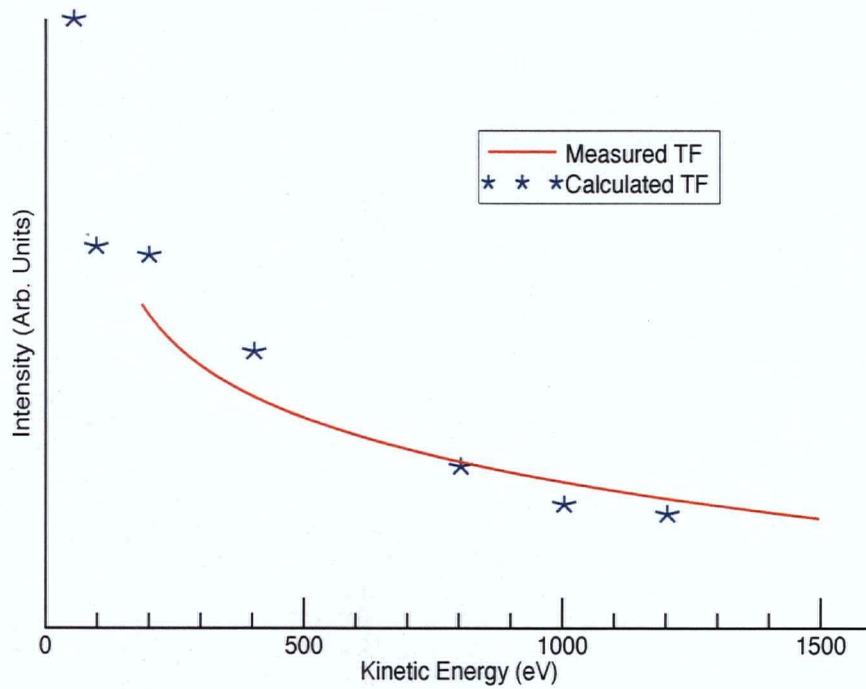
Figure 2.11: Comparison of the measured and calculated transmission function for FAT mode, medium magnification lens setting, pass energy 40 eV and Iris 15. The measured transmission function agreed well with the calculated one. The calculation was performed by SPECS.
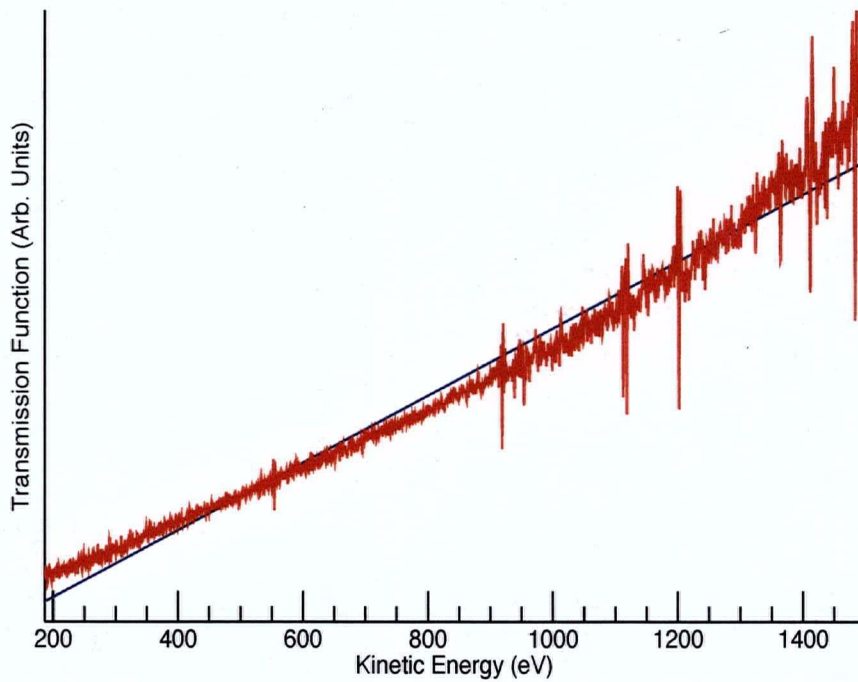
Figure 2.12: Measured FRR transmission function for Medium Magnification, Retard Ratio 20 and Iris 15. The measured spectra deviates form the expected linear behaviour. This is the most probably reason for the failure of Method I, as the method is based on this assumption.

Sets of data taken with conservative powers and analyzer settings for XPS measurements have shown non-linearities in their intensity response. The method presented was successful in removing these non-linearities from the data. This procedure should be used before performing any quantitative peak analysis, including measuring the transmission function of the analyzer. This correction created a 1% improvement in measurements of relative chemical abundance of the $SrCuO_2$ films.

Two methods were used to measure the transmission function of the analyzer. The first method, the FAT/FRR method, was been found to rely on an incorrect assumption of a linear transmission function in FRR mode. The second method, the transmission function from peak intensities, has been successfully used to determine the analyzer's transmission function. The measured transmission function was found to agree well with the calculated transmission function provided by SPECS (making almost no difference in the measured stoichiometry of the $SrCuO_2$ films). Using this measured transmission function, it was also demonstrated that the FRR mode of this analyzer does not have a linear transmission function, and that this was the most likely cause of the failure of FAT/FRR method.

Correcting the non-linearities of the detector is a necessary step in performing any quantitative peak analysis with this analyzer. Measuring the transmission function may not be a necessary step, however, as long as a calculated transmission function is used. Not correcting for the transmission function at all introduces significant errors, on the order of $2 - 3\%$. These types of corrections will be necessary in future to ensure the quality of the $SrCuO_2$ films is high enough to perform a meaningful ARPES study.

Chapter 3

Growth of $SrCuO_2$

3.1 Introduction

Growing $SrCuO_2$ films epitaxially offers some advantages over conventional
bulk growth. For instance, epitaxial growth results in a very thin sam-
ple composed primarily of surface atoms and a flat surface suitable for an
ARPES or STM study. This growth technique makes it possible to perform
these surface sensitive measurements on wider variety of materials (ones
that do not cleave to expose a flat surface). Unfortunately, the structural
and chemical probes available for thin film samples are severely limited.
This can be a problem due to the high sample quality required to extract
meaningful information from the materials. The thinness of the film makes
normal bulk sensitive probes much less accurate or impossible. However,
there are several options for examining the structure and chemistry of films.
The majority of these techniques rely on the short mean free path of elec-
trons in solids to probe only the surface of the material. Techniques such as
electron diffraction and X-Ray Photoelectron Spectroscopy (XPS) can probe
the structure and and chemistry of a thin film without being influenced by
the substrate. In this chapter, the growth of $SrCuO_2$ films is discussed,
followed by a discussion of the results of Reflection High Energy Electron
Diffraction (RHEED) and XPS characterization measurements.

3.1.1 Molecular Beam Epitaxy

The goal of thin film crystal growth is to form a thin film of single crys-
talline material through some deposition process on a suitable single crystal
substrate. To have epitaxial growth, the film and substrate must have their
lattice constants and crystal symmetry match at the interface between them
(as opposed to thin film crystal growth, where there does not need to be any
lattice matching). In this thesis, the technique of Molecular Beam Epitaxy
(MBE) is used to prepare epitaxial $SrCuO_2$ thin films.

MBE is a Physical Vapour Deposition (PVD) technique. The MBE
technique involves the evaporation of elemental sources in an ultra-high

vacuum environment. Sources are heated, whether with an electron beam, a laser or directly (using a Knudsen cell), until their vapour pressure is high enough to allow a reasonable amount of material to traverse the distance between the source and the substrate. The low pressure of the growth chamber means that the evaporated material has a very long mean free path (many times larger than the sample/substrate distance). The evaporated material is collimated, producing a "molecular beam" that impinges the sample. The rate of evaporation can be precisely controlled to an accuracy of less than a mono-layer of deposited atoms and the resulting films are extremely clean, due to the ultra high vacuum environment.

Removed Pending Copyright Permission

Figure 3.1: The Oxide MBE in the Quantum Materials Laboratory at UBC (from [22])

The Oxide MBE in the Quantum Materials Laboratory is a system custom designed with simplicity, modularity and connectivity in mind. The sample holding system is compatible with the lab's ARPES chamber and transfer chamber, allowing films to be transported from the growth chamber to the analysis chamber without breaking the vacuum. Sources include several Knudsen cells with various temperature capabilities, a Mantis Deposition RF Atom Source, a sputter gun and several gas leak valves. Rates are monitored with a Quartz Crystal Monitor (QCM) on a custom designed stage that flips to expose the sample to the molecular beams. Until re-

cently, substrate heating was accomplished with filaments incorporated into the sample holder. Substrates are now heated by a custom external CO_2 laser system and temperatures are measured with a pyrometer. A high energy electron gun and detection system are used to measure Reflection High Energy Electron Diffraction (RHEED) patterns (explained in section 3.2.1).

Molecular Beam Epitaxy Vs. Pulsed Laser Deposition

The majority of the work done on the growth of oxide thin films has utilized the technique of Pulsed Laser Deposition (PLD) to grow samples, another type of PVD. In this process, a high power laser (normally a KrF excimer laser) is fired repeatedly into a sintered target made of the film material. The target material is vaporized and travels through the vacuum to form a film on the substrate. The rate of deposition is controlled by changing the lasers firing rate. The difference between PLD and laser MBE is that the PLD target is a composite material with the same stoichiometry as the desired film, while the laser MBE target is an elemental source that will react with other materials at the substrate surface to form the desired film. The primary advantage of the PLD process is its simplicity.

The disadvantage of the PLD technique, and the reason it was not used for this work, is that the laser/target interaction and its effect on the vaporized material is very complicated and poorly understood. The process creates an ionized plasma plume at the laser impact site, and the nature of the ablated units is unknown. This presents possible problems for performing APRES measurements on the samples in the future. The sample quality requirements are very stringent in APRES, and in an attempt to avoid possible complications arising from the unknown nature of the ablated units, the MBE technique is used.

3.2 Experimental

3.2.1 Reflection High Energy Electron Diffraction

Reflection High Energy Electron Diffraction (RHEED) is an electron diffraction technique that can be used during film growth. High energy electrons are fired at the sample at a glancing angle, and a phosphour screen on the other side of the chamber is used to collect the reflected diffraction pattern.

The diffraction pattern produced by RHEED satisfies the normal conditions for diffraction (the Bragg condition, or the Ewald construction) except that only the in plane lattice parameters are probed. This is due to the

short mean free path of electrons in the crystal perpendicular to the surface. While the electrons energy is high, and one would expect a deeper penetration, the electrons only hit the surface at a glancing angle therefore do not penetrate very far. This implies that the reciprocal lattice that is sampled is 2-D. The diffraction pattern exhibits "stripes" as a result (see Figure 3.3). This can be explained qualitatively by realizing that, in the plane, the electrons sample a large area, with many diffraction planes, resulting in discrete points when switched to reciprocal space. Out of the plane, however, the electrons sample only a short distance, resulting in an extended rod when switched to a reciprocal space representation.

Figure 3.2: A RHEED diffraction pattern of a Mica sample. The 2-D nature of the diffraction pattern is evident in the extended, rod-like nature of the diffraction spots.

Traditionally, RHEED is used to monitor growth rate by measuring oscillations in the intensity of the diffracted pattern. A perfectly flat surface will produce the maximum diffracted intensity. As material is deposited on that surface, the flat surface begins to roughen and the intensity of the beam lessens as the scattering becomes increasingly diffuse. As a full mono-layer of material is deposited, the surface becomes flat again (assuming 2-D growth), and the intensity reaches another maximum. The period of oscillation of the RHEED pattern corresponds to the rate of mono-layer growth.

Removed Pending
Copyright Permission

Figure 3.3: An explanation of RHEED oscillations. As the atomically flat surface begins to roughen, the amount of diffuse scattering of the electron beam decreases to a minimum corresponding to maximum surface roughness. As the amount of material deposited begins to approach that required for a full mono-layer, diffuse scattering decreases and the RHEED intensity increases to a maximum corresponding to a full mono-layer deposited. From [23]

RHEED can also be used to extract crystallographic information. Normally, only one direction of the crystal is probed by the beam. The change in one lattice parameter relative to its corresponding substrate parameter can be monitored as a function of time (see figures 3.8 and 3.9). It is possible, however, to take RHEED images at various angles and reconstruct the 2-D reciprocal lattice of the surface. This provides information similar to Low Energy Electron Diffraction (LEED), except that the data can be taken during crystal growth. This is particularly useful for observing changes in crystal symmetry or changes in lattice parameter at different stages of growth [22] (an example is given in figure 3.4). While this technique is not used in this thesis, it is mentioned because it promises to be an invaluable tool in later growths of $SrCuO_2$ films.
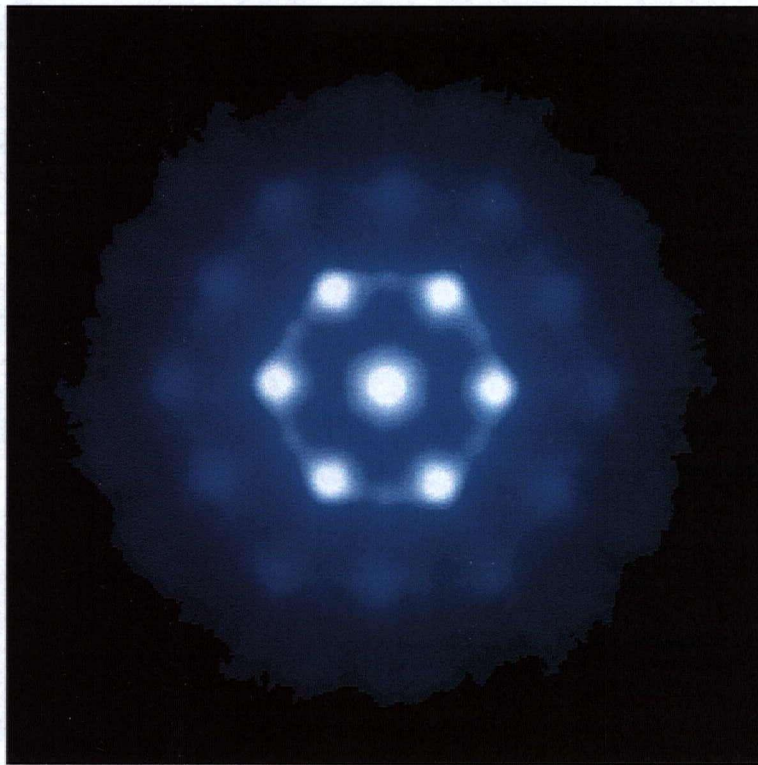

Figure 3.4: *Au* (111) surface reciprocal lattice reconstructed from RHEED data. The pattern has the expected symmetry for a (111) *Au* surface.

3.2.2 X-Ray Photoelectron Spectroscopy

XPS measurements involve exposing the sample under study to X-ray radiation from an X-ray source or synchrotron light source and collecting the photo-emitted electrons. An example spectra is shown in figure 3.6. The kinetic energy of the photo-emitted electrons is given in the simplest approximation by equation 3.1.

$$E_k = \hbar\omega - \phi - E_B \qquad (3.1)$$

Removed Pending
Copyright Permission

Figure 3.5: Pictorial description of the photo-emission process. An incoming photon of energy $\hbar\omega$ excites electrons out of their bound levels in the solid and promotes them to empty vacuum levels (from [12]).

E_k is the kinetic energy of the photo-emitted electrons, $\hbar$ is Planck's constant, ω is the photon frequency ($\hbar\omega$ is the energy of the photon), and
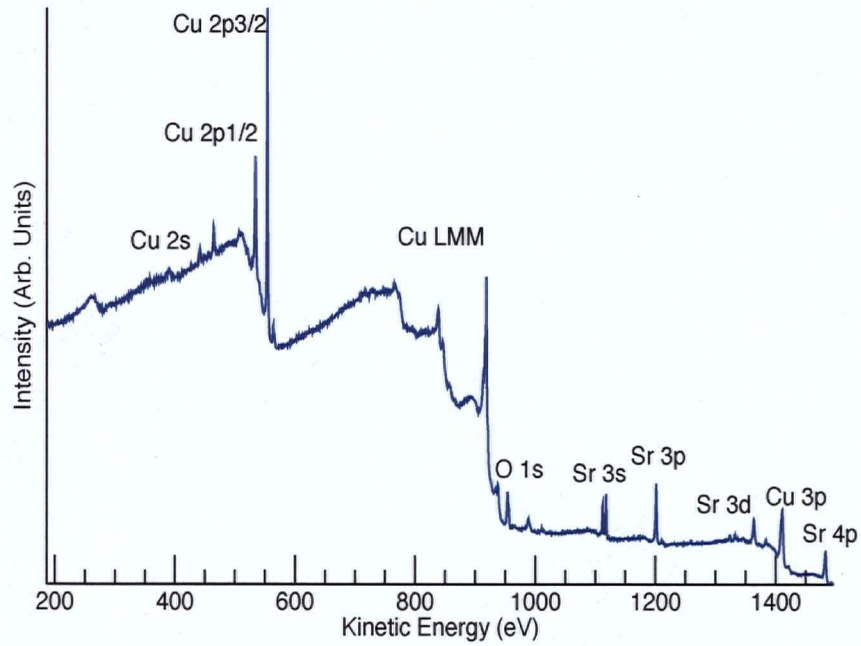
37

Figure 3.6: An example XPS scan of a $SrCuO_2$ Sample. This spectra can be used to extract many different quantiites, including the oxidation level of the Cu and the relative concentrations of Sr and Cu.

E_B is the binding energy of the electron (measured relative to E_f, the Fermi energy). ϕ is the work function of the material (the difference between the vacuum level and E_f) and is included because of the convention of measuring binding energies from the Fermi level and not the vacuum level. This is process is demonstrated pictorially in figure 3.5.

A more accurate way of representing the photo-emission process is the following:

$$E_k = \hbar\omega - \phi - (E_f^{N-1} - E_i^N) \qquad (3.2)$$

Now, instead of the binding energy, the kinetic energy depends on the difference between the energies of the final state of the system with one electron removed (E_f^{N-1}) and the initial N electron state (E_i^N)(N is on the order of Avagadro's Number). Fortunately, for XPS data where core level information is the most important, one can usually use the relation in equation 3.3.

$$E_B = (E_f^{N-1} - E_i^N) \qquad (3.3)$$

This gives us back equation 3.1 when substituted into equation 3.2. In systems where electronic correlations are important, however, one must take into account the possibility that the core hole left behind by the photo-emission process can interact with other particles in the system. Then, equation 3.2 must then be used.

This description of the photo-emission process is suited to a scientist interested in understanding the details of the electronic structure of the material. For a film grower who is more interested in characterizing their samples, an experimental description of the photo-emission process is more appropriate. The intensity of a photoelectron peak is given by equation 3.4 [21, 24].

$$I = xf\sigma(E_k)\phi y AT(E_k)F(E_k) \qquad (3.4)$$

Where x is the atomic concentration, f is the x-ray flux, E_k is the electron kinetic energy, $\sigma(E_k)$ is the photoelectron cross section, ϕ is the instrumental geometry factor (a function of the angle between the photon beam and the detector, normally constant), y is the efficiency factor for the production of a photoelectron that leaves the system in the N-1 system

ground state, A is the area from which the photoelectrons are emitted, $F(E_k)$ is the mean free path of the photoelectrons in the sample, and $T(E_k)$ is the transmission function of the analyzer. All of the physics based initial and final state energy considerations are lumped into $\sigma(E_k)$ and y, leaving the experimentalist free to deal with the other terms in equation 3.4.

Extracting Chemical Information From XPS

When one wants to extract chemical information, the relevant quantity is the atomic concentration x from equation 3.4. This is normally extracted from the peak area or from intensity through tabulated atomic sensitivity factors

$$S = \sigma(E_k)\phi y A T(E_k) F(E_k) \qquad (3.5)$$

$$I = x f S \qquad (3.6)$$

Each peak intensity is divided by the appropriate atomic sensitivity factor, and then all the peaks for each element are added together. Only relative concentrations can be determined in this manner, as the unknown x-ray flux f must be divided out.

The disadvantage of using tabulated atomic sensitivity factors is that, at best, they are only valid for a single set of analyzer settings. The transmission function $(T(E_k))$ is very sensitive to the settings used by the analyzer, and can vary between analyzers from the same manufacturer. It also changes as a function of time [25, 26]. A better method would be to deal with each term in equation 3.4 individually. A and ϕ are constants at fixed photon energy and are independent of the chemical species being analyzed. If all of the satellites around the main peak are included in the intensity of the main peak, then y goes to 1. One can use calculated σ values for each photoelectron peak [24]. $F(E_k)$ has an approximate functional form ($\propto \sqrt{E_k}$ in the XPS limit [19]). The transmission function, $T(E_k)$, must be measured (see Section 2.2.2).

Determining Oxidation Level of Cu with XPS

As is discussed in Section 4.1.1, proper oxidation of the grown films is the most difficult part of growing $SrCuO_2$ epitaxially. XPS is used in this thesis to measure the oxidation of the Cu (Sr has only one oxidation level and is trivial to oxidize properly relative to the Cu). It is possible to determine the oxidation level of Cu by measuring small shifts in the binding energy

of various photo-electron peaks, but in the case of Cu, a more accurate technique is possible. The correlated nature of CuO and the effect that it has on its core level spectrum is used to differentiate it from Cu_2O, which is well described by a single electron, non-interacting approach (this is an instance where the assumption used in equation 3.1 fails, and equation 3.2 must be used).

Cu metal has a valence configuration of $3d^{10}4s^1$. At its most accessible oxidation, 1+, it forms Cu_2O, and the valence configuration of the Cu becomes $3d^{10}$. In terms of photoemission, this means that there is only one peak that will be measured when an electron is photo-excited (ignoring the possibility of multiplet splitting). For the higher oxidation level of Cu, 2+ (forming CuO), there are two possible initial state levels. The obvious possibility is $3d^9$, but there is also the option of a charge transfer from the ligand Oxygen, creating a $3d^{10}\underline{L}$ state ($\underline{L}$ represents a ligand hole). In this instance, the linear combination of two initial states creates 2 possible peaks in the spectrum (See Figure 3.7), a main line, and a shake-up satellite.

This presents several ways of determining the oxidation level of the Cu. One method uses the ratio of cross sections of $\frac{\sigma(O2p)}{\sigma(Cu3d)}$ in the valence band. While this works well at low photon energies (He II and He I), the cross section ratio for $Al\,K\alpha$ X-ray radiation is very small (0.02)(predominantly d character) and hence not suited for XPS measurements of oxidation. For XPS, the best way is to measure the ratio of peak area intensities of the $Cu\,2p_{\frac{3}{2}}$ peak and its shake-up satellite. This ratio of $\frac{I_{sat}}{I_{main}}$ is 0.55, and the intensity of both peaks is very strong and easy to measure [12, 28].

3.3 Results

In total, three growths were completed. Several more were attempted, but were unsuccessful due to equipment failures, which in some cases required several weeks to fix. The details of the growths are outlined in table 3.1

RHEED time series for each of these samples all showed similar behaviour. At the start of growth, the films all began to display 3-D style growth, characterized by discrete spots in the RHEED diffraction pattern as opposed to extended rods. The behaviour quickly disappeared and was replaced with a 2-D style growth. For growth #1, the lattice parameter changed suddenly from 3.905 Å measured along the (100) direction of the $SrTiO_3$ substrate to 1.760 Å (see figure 3.8). Growths #2 and #3 did not exhibit this change in lattice parameter, indicating possible epitaxial growth (data for all lattice parameters is needed to say this conclusively).
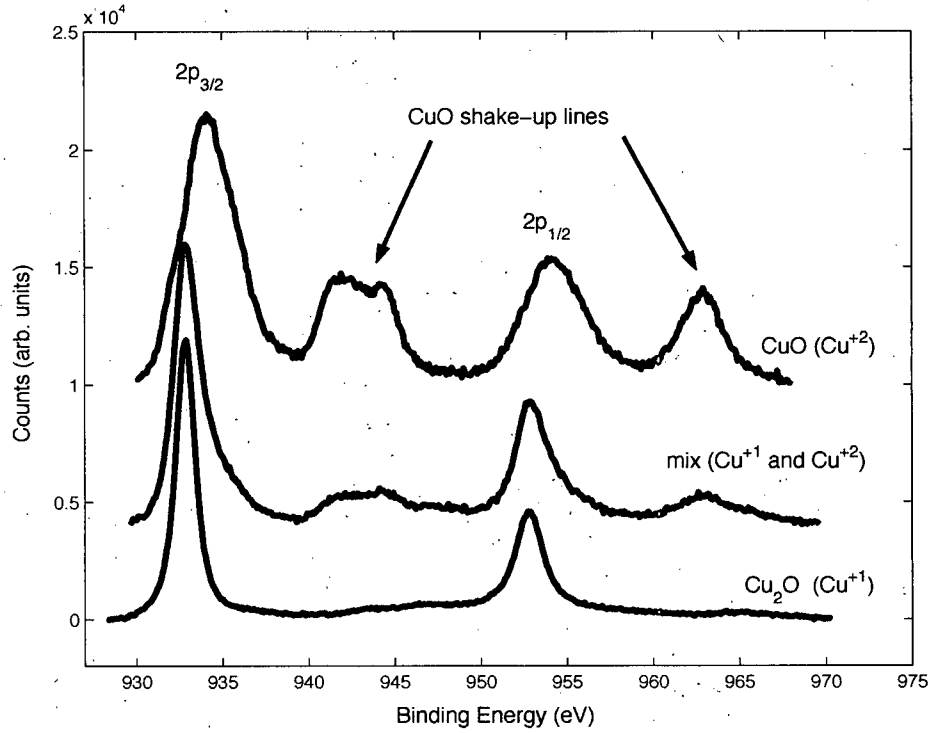
Figure 3.7: Comparison of CuO and Cu_2O 2p structure. The two peaks in the CuO $2p_{\frac{3}{2}}$ shake-up lines are due to multiplet splitting of the higher binding energy $3d^9$ level (from [27]).

Growth #	Substrate Temperature (^oC)	Deposition Rate $\left(\frac{\overset{o}{A}}{min}\right)$	Oxygen Pressure (Torr)	$\frac{Sr}{Cu}$ Ratio	Oxidation Level ($\frac{I_{sat}}{I_{main}}$) (0.55 = 100%)
1	620	10	1.2×10^{-6}	0.82	0.05
2	608	5	1.0×10^{-6}	1.14	0.06
3	545	6	5.9×10^{-7}	0.85	0.05

Table 3.1: Summary of growth parameters for $SrCuO_2$

The largest difference between growth #1 and growths #2 and #3 is the deposition rate. A lower deposition rate appears to be more conducive to growth with a matched lattice. There were no visible RHEED oscillations during any of the growths. This data suggests that the substrate surface had some atomic scale roughness to it, and that the film initially grew in a 3-D fashion to compensate for this. A new substrate preparation technique has been implemented which leaves the $SrTiO_3$ substrates with an atomically flat surface; this should alleviate this problem.
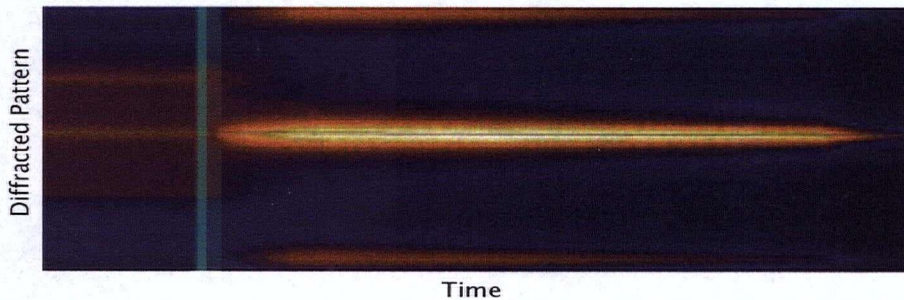

Figure 3.8: RHEED time series for a $SrCuO_2$ growth #1. The vertical axis is the diffraction pattern and the horizontal axis is time. The start of the growth is indicated by the shaded area. The signal before the start of growth is that of $SrTiO_3$, and the signal after the growth is that of an unknown phase. The change in reciprocal lattice spacing corresponds to a lattice parameter change from 3.905 Å to 1.760 Å.

XPS data from all of the samples indicate that none of the films were properly oxidized (predominantly Cu_2O with a small amount of CuO). The peak height ratio is so small that increasing the O_2 pressure to the maximum possible operating pressure of the oxide MBE chamber will not properly oxidize these films. A different substrate temperature, along with a more reactive species of Oxygen will be necessary to properly oxidize the films. As a result, in Chapter 4, the effectiveness of an atomic Oxygen source is determined.

XPS data also indicates that the ratio of $\frac{Sr}{Cu}$ was not correct in any of the growths. For equal deposition rates of each element, small changes in other growth parameters caused the stoichiometry to vary wildly. Fortunately, the rate at which material is deposited is much easier to control than any other parameter in the growth, and can be tuned easily after all of the other variables (such as oxidation) are correct.
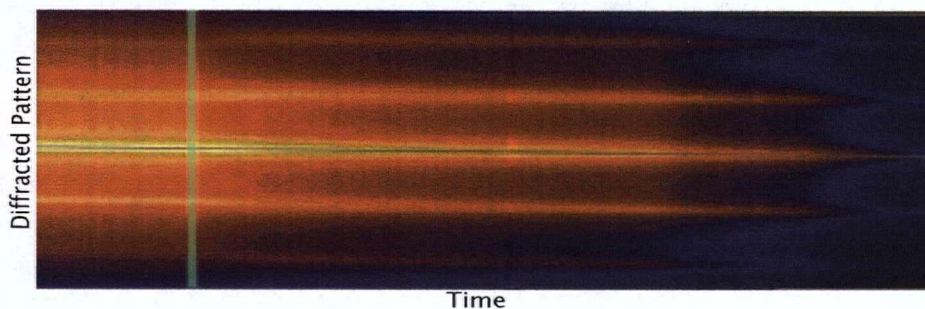
Figure 3.9: RHEED time series for a $SrCuO_2$ growth #3. The vertical axis is the diffraction pattern and the horizontal axis is time. The start of the growth is indicated by the shaded area. The signal before the start of growth is that of $SrTiO_3$, and the signal after growth is that of a material with the same lattice parameter. The RHEED time series for sample #2 was similar.

3.4   Conclusions

Despite several attempts, $SrCuO_2$ epitaxial films were not grown successfully on $SrTiO_3$ substrates. The RHEED patterns taken during growth all show the same initial 3-D growth, and then switch to a 2-D growth pattern. A possible reason for this behaviour is that the $SrTiO_3$ substrates have a poor surface quality, and hence the films initially grow in a 3-D manner. This will be dealt with in future growths with a new substrate preparation procedure. Low evaporation rates ($\sim 5 \left(\frac{\overset{\circ}{A}}{min} \right)$) produced potentially epitaxial films, while high deposition rates cause a new phase to be formed. The stoichiometry of the films varied between each growth despite equal deposition rates of the Sr and Cu. This is not a major issue due to the ease of altering the rate of deposition after all of the other growth parameters have been established. In all cases, the level of oxidation of the film was inadequate. Chapter 4 deals with the calibration of an atomic Oxygen source, and its applicability for oxidizing $SrCuO_2$ films. A new sample heating mechanism in the Oxide MBE chamber will make it possible to increase the temperature of the film to higher values in future growths. This will also help to increase the oxidation level of the films.

What has been learned in these preliminary growths will ensure that future films will be grown with the correct structure and chemistry. All

44

of the difficulties encountered here are surmountable. The work that has been done to improve the utility of RHEED data [22], the quality of the substrate's surface, the range of the sample heating mechanism and the accuracy of XPS data will ensure that subsequent growths of this material will yield samples of high enough quality to perform meaningful ARPES measurements on.

Chapter 4

Creation of Atomic Oxygen

4.1 Introduction

In the previous chapter, it was found that molecular Oxygen (O_2) was not reactive enough to properly oxidize the $SrCuO_2$ films. To rectify this, a more reactive form of Oxygen is needed. This chapter deals with the calibration of a Mantis Deposition MATS30 RF Atom Source for creating Atomic Oxygen (AO), in the hope that it can be used to drive the oxidation of the $SrCuO_2$ films to the required levels.

4.1.1 Creation of Atomic Oxygen

The conventional bulk growth of $SrCuO_2$ requires both high pressure and a high oxidation level to grow successfully. The pressure cells used in the growth provide enough heat and pressure to satisfy both of these requirements. In epitaxial growth, the substrate lattice matching provides the required strain/pressure, but reaching the proper oxidation level is difficult in a low pressure MBE system. Properly oxidizing the films is, in fact, the most difficult part of growing $SrCuO_2$.

$SrCuO_2$ can be regarded for the purposes of oxidation as a mixture of SrO and CuO. Formation of SrO is trivial, as Sr readily reacts with Oxygen, and has only one available oxidation level of 2+. The formation of CuO is much more difficult. The most accessible oxidation level for Cu is 1+, which forms Cu_2O when exposed to oxygen. Reaching the 2+ oxidation level for Cu requires high pressures of O_2 (which is impossible in a vacuum environment), high temperatures for the Cu, and/or a more reactive species of Oxygen.

It is possible to raise the temperature of the sample to increase the oxidation level of the material, but in thin film growth, the vacuum environment and presence of the substrate can complicate matters (for example, the deposited film can re-evaporate off of the substrate, or the substrate can undergo a change of phase). An element where we have more control is the reactivity of the Oxygen. Ozone (O_3) and Nitrous Oxide (NO_2) have

both been used previously to increase the reactivity of the Oxygen to the point where CuO films can be grown, but both gases are hazardous and require special handling and pumping procedures [29, 30]. Additionally, the possibility that Nitrogen could be included in the film when Nitrous Oxide is used makes this approach even less desirable. An alternative is to use a source of Atomic Oxygen (AO). Molecular Oxygen is fed into a device that breaks apart O_2 and ideally produces a stream of AO, free of any ions. There are two methods of achieving this. The first involves thermal cracking of O_2 over a hot metal surface. This is a common practice for cracking non-reactive gases, but becomes more difficult due to the reactive nature of the Oxygen (some sources designed specifically for cracking Oxygen do this effectively with a hot Platinum surface). The other method involves running O_2 through a Radio Frequency (RF) or microwave cavity. The frequency is tuned to produce a standing wave in the cavity that tears apart the O_2 and creates a plasma of AO ions. These AO ions quickly take an extra electron from any available source and are allowed to leak out of the cavity into the vacuum chamber. The resultant beam of AO is directed at the sample. Any free ions that escape can be removed from the beam by deflecting them with an electrostatic field.

The method of creating an Oxygen plasma with a RF source is investigated in this thesis. As the success of growing $SrCuO_2$ epitaxially depends on properly oxidizing the films, the cracking efficiency of the source must be determined and compared with devices that have been used previously to grow $SrCuO_2$ films.

4.2   Experimental

The method used in this thesis to measure the amount of AO produced by a Mantis Deposition MATS 30 RF Atom Source (using a quartz tube with 6 holes escape holes as the plasma cavity) involved measuring the rate of increase of mass of a silver film deposited on a QCM exposed to AO. Molecular O_2 does not diffuse into a Ag film, but AO does. The rate of AO atoms impinging on the substrate can be can be measured with a QCM by measuring the rate of thickness/mass increase of the film as a function of time [27, 31].

The rate of AO diffusion into the film increases the measured QCM thickness as an inverse exponential function of time.

$$T(t) = A_o - B_o e^{-\lambda t}$$ (4.1)

Where T(t) is thickness as a function of time, A_o is the final film thickness when the Ag film is saturated with AO, B_o is the difference between the initial and final thickness of the film, and λ dictates the rate at which the film increases in thickness. Differentiating 4.2 gives us the rate of thickness increase:

$$\frac{dT(t)}{dt} \;=\; B_o \lambda e^{-\lambda t} \tag{4.2}$$

The rate of diffusion into the film is a maximum at t=0, giving an initial rate of $B_o\lambda$, with units of $\frac{thickness}{time}$. It must be remembered that this measured thickness does not actually represent the thickness of the film. The QCM measures thickness by measuring the change in resonant frequency of an oscillating quartz crystal, which changes as more mass is accumulated on the film. What is needed is a conversion from thickness to number of AO molecules. This is given by equation 4.4.

$$AO \; Rate \;=\; \frac{\rho_{Ag}}{m_{AO}}(B_o\lambda) \tag{4.3}$$

$$AO \; Rate \;=\; 3.948 \times 10^{15}(B_o\lambda) \qquad (\frac{atoms}{s \; cm^2}) \tag{4.4}$$

ρ_{Ag} is the density of Ag and m_{AO} is the mass of AO. $(B_o\lambda)$ are measured from fits of the QCM data. It should be noted that the initial rate of absorbed AO may not be the actual rate of AO impinging on the sample; there is no way to tell if all of the AO is actually absorbed by the Ag film. This information is still useful, however, if the measured rates are compared to the rates of other sources of AO measured in the same way. Additionally, understanding the behaviour of the source under different conditions ensures that it is used to its greatest possible effect.

4.3 Results

For each measurement, $200nm$ of Ag were evaporated onto an Au QCM. The films were exposed to molecular O_2 to ensure that the molecular species would not affect the measurement. Closing the shutter on the AO source while in operation successfully stopped the Ag film from absorbing AO while the plasma was lit. QCM thickness measurements were taken as a function of time, sampling every 6 seconds. The thickness/time data was fit to a function of the form equation 4.2 to determine A_o, B_o and λ.

The first study looked at the oxygen flux as a function of power at constant pressure/flow rate. The results are presented in figure 4.1.
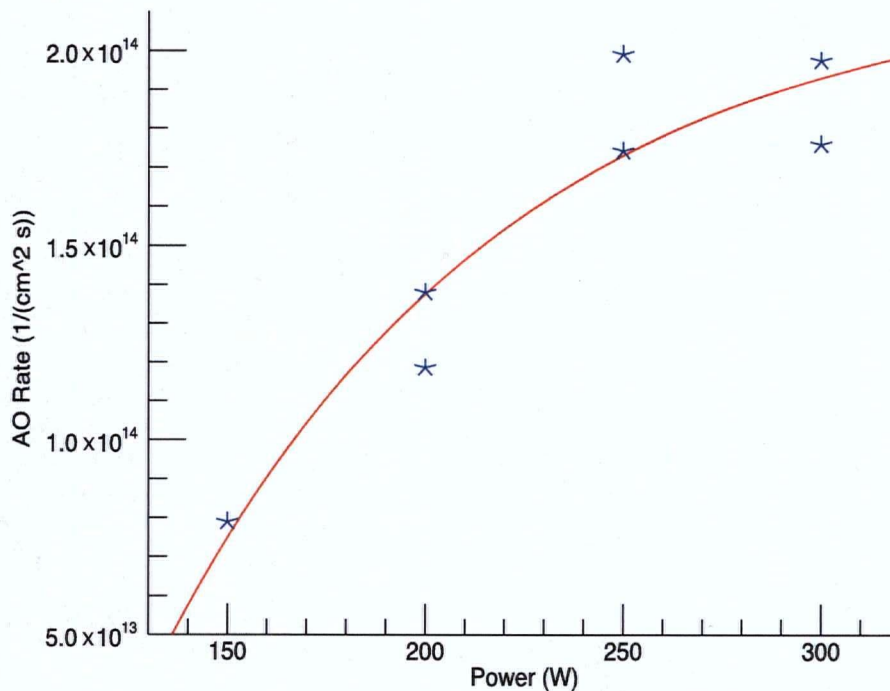

Figure 4.1: Flux of AO as a Function of Power at a Constant O_2 Pressure of 6.2×10^{-6} Torr (1.1 sccm Throughput).

These results fit better to an inverse exponential function than to a linear function, implying that the AO rate is saturating as more power is introduced. While there is too little data to fit the function properly, a rough estimate of the maximum possible AO rate from the fit is $2.2 \times 10^{14} \frac{atoms}{cm^2 s}$ at a flow rate of 1.1 *sccm*.

The second part of this study involved measuring the cracking efficiency of the atomic source as a function of increasing Oxygen pressure. The power of the source was kept at 250 W. The range of pressures chosen covered the span between where the plasma was just able to sustain itself (2.7×10^{-6} Torr or 0.5*sccm*) to close to the maximum pressure allowed by the Oxide MBE chamber interlock (4.1×10^{-5} Torr or 7.4 sccm).

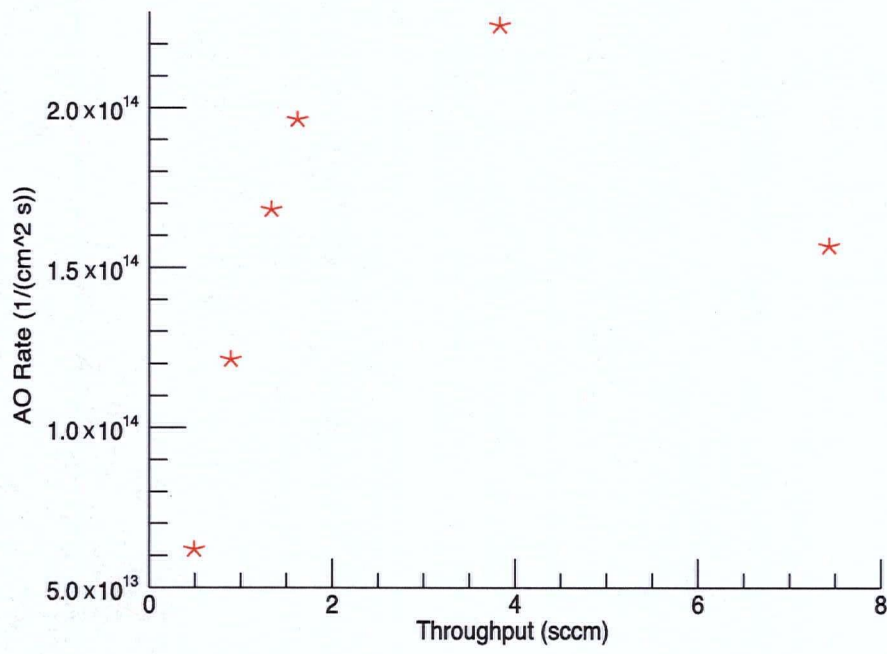The data in figure 4.2 suggests that the maximum rate of AO flux is

Figure 4.2: Flux of AO as a Function of Throughput at a Constant Power of 250 W

achieved at 250 W at a flow rate of between 2 and 6 sccm. If the trend suggested by the rate versus power data at low Oxygen throughput, shown figure 4.1, holds for higher Oxygen throughputs, then it would be reasonable to expect that rates on the order of $10^{15} \frac{atoms}{cm^2 s}$ are possible with this source.

A future extension of this study would be to investigate the AO flux versus power at Oxygen flow rates in the high cracking efficiency range seen in 4.2, as well as filling gaps in the data presented in figure 4.2. Another possible extension that would increase the utility of the AO source would be to use this information to calibrate a system that could be used to measure AO rates during crystal growth. For example, a hot Platinum wire placed in the AO stream could be used to measure the rate of recombination of the AO as it strikes the Platinum surface. As the AO recombines on the surface, a certain amount of heat is generated, which changes the resistance of the wire. This change of resistance is proportional to the amount of AO flowing over the surface of the wire.

4.4 Conclusions

The Oxygen cracking efficiency of a Mantis Deposition RF Atom Source has been determined. AO rates in the range of $8 \times 10^{13} \frac{atoms}{cm^2 s}$ to $2.4 \times 10^{14} \frac{atoms}{cm^2 s}$ have been demonstrated. AO rates on the order of $10^{15} \frac{atoms}{cm^2 s}$ are deemed possible, but the nature of the cracking efficiency of the plasma is poorly understood; further study is required to confirm this.

These results are comparable to other sources whose rates were measured in the same way. For example, 100W at 10 sccm yielded $3.5 \times 10^{15} \frac{atoms}{cm^2 s}$ for a microwave plasma source [27], and similar AO rates at 1.0 Torr of pressure for another microwave source [32]. It is difficult to make a direct comparison, however, due the fact that the Oxygen pressures involved were higher than achievable here in both cases.

Whether this source is appropriate for properly oxidizing $SrCuO_2$ films still needs to be determined. Rates of $5 \times 10^{16} \frac{atoms}{cm^2 s}$ have been found necessary to properly oxidize copper in a related material $SrCu_2O_3$ [27], but these values were measured using atomic absorption techniques and are not necessarily comparable to QCM based measurements.

Chapter 5

Conclusions

In this thesis, preliminary growths of $SrCuO_2$ epitaxial films were undertaken. Despite none of the growths yielding the desired stoichiometry or oxidation, the difficulties that were encountered, such as properly oxidizing the film, are demonstrated to be surmountable. The structure of the films was probed with RHEED, and found to display growth patterns that are consistent with epitaxial growth. The lessons learned from these attempts will make it possible to grow an epitaxial film of $SrCuO_2$ for an ARPES study in the future.

The strict sample quality requirements imposed by a future ARPES study, and hence the need for the most accurate measurements of stoichiometry possible, warranted an investigation of the properties of the SPECS PHOIBOS 150 hemispherical electron analyzer used to perform XPS measurements of films chemistry. The degree of non-linearity of the electron detection system was determined and a method introduced that could correct for it. Correcting the data for the transmission function of the analyzer was found to be a necessary step in performing quantitative chemical analysis ($2 - 3\%$ differences were observed in stoichiometry before and after applying the transmission function). Therefore, the transmission function of the analyzer was measured using two techniques. The measured transmission function agreed well with calculated transmission functions provided by SPECS (the difference in $SrCuO_2$ film stoichiometry being less than 1% between the 2 transmission functions). While correcting for detector non-linearity and measuring the actual transmission function did not drastically alter the stoichiometry measurements for scans taken using reasonable analyzer settings for XPS (about 1%, mostly from detector non-linearity), it is possible to drive the analyzer into regimes where the corrections would be necessary. The methods used to first correct for the intensity response of the analyzer, and then the transmission function would be more applicable in these instances.

This work constitutes the first steps towards an ARPES study of the electronic properties of $SrCuO_2$ films. The possibilities offered by epitaxial growth, such as structural tuning through lattice matching, or electronic

reconstruction through substrate/film interactions, will be exploited to alter the films properties. This will make it possible to not only to study the properties of $SrCuO_2$ using a surface sensitive measurement technique (which before now was not possible), but also to investigate novel methods of tuning the properties of the TMOs. This study aims to shed light on the nature of electronic correlations in these materials, and investigate new ways to control their properties.

Bibliography

[1] KJ Franke, P. Gille, KH Rieder, and W. Theis. Achieving Epitaxy between Incommensurate Materials by Quasicrystalline Interlayers. *Physical Review Letters*, 99(3):36103, 2007.

[2] A. Zangwill. *Physics at Surfaces*. Cambridge University Press, 1988.

[3] NJC Ingle, RH Hammond, and MR Beasley. Molecular beam epitaxial growth of $SrCu_2O_3$: Metastable structures and the role of epitaxy. *Journal Of Applied Physics*, 91(10), 2002.

[4] A. Vailionis, A. Brazdeikis, and AS Flodström. Observation of local oxygen displacements in CuO_2 planes induced by a misfit strain in heteroepitaxially grown infinite-layer-structure $Ca_{1-x}Sr_xCuO_2$ films. *Physical Review B*, 55(10):6152–6155, 1997.

[5] MA James and T. Hibma. Thickness-dependent relaxation of NiO (001) overlayers on MgO (001) studied by X-ray diffraction. *Surface science*, 433:718–722, 1999.

[6] WA Harrison, EA Kraut, JR Waldrop, and RW Grant. Polar heterojunction interfaces. *Physical Review B*, 18(8):4402–4410, 1978.

[7] R. Hesper, LH Tjeng, A. Heeres, and GA Sawatzky. Photoemission evidence of electronic stabilization of polar surfaces in K_3C_{60}. *Physical Review B*, 62(23):16046–16055, 2000.

[8] N. Nakagawa, H.Y. Hwang, and D.A. Muller. Why some interfaces cannot be sharp. *Nature Materials*, 5(3):204–209, 2006.

[9] A. Ohtomo, DA Muller, JL Grazul, and HY Hwang. Artificial charge-modulationin atomic-scale perovskite titanate superlattices. *Nature*, 419(6905):378–380, 2002.

[10] N. Reyren, S. Thiel, AD Caviglia, L. Kourkoutis, G. Hammerl, C. Richter, CW Schneider, T. Kopp, A.S. Ruetschi, D. Jaccard,

et al. Superconducting Interfaces Between Insulating Oxides. *Science*, 317(5842):1196, 2007.

[11] C. Freysoldt, P. Rinke, and M. Scheffler. Ultrathin oxides: bulk-oxide-like model surfaces or unique films? *Physical Review Letters*, 99(8):086101, 2007.

[12] Stefan Hüfner. *Photoelectron spectroscopy : principles and applications*, volume 82 of *Springer series in solid-state sciences*. Springer-Verlag, Berlin ; New York, 2nd edition, 1996.

[13] A. Damascelli, Z. Hussain, and Zhi-Xun Shen. Angle-resolved photoemission studies of the cuprate superconductors. *Reviews of Modern Physics*, 75(2):473–541, 04 2003.

[14] SPECS GmbH. *PHOBIOS Hemispherical Energy Analyzer Series*, 2.08 edition.

[15] N. Mannella, S. Marchesini, AW Kay, A. Nambu, T. Gresch, SH Yang, BS Mun, JM Bussat, A. Rosenhahn, and CS Fadley. Correction of non-linearity effects in detectors for electron spectroscopy. *Journal of Electron Spectroscopy and Related Phenomena*, 141(1):45–59, 2004.

[16] SPECS GmbH. *PHOBIOS CCD Imaging Detector*, 1.13 edition.

[17] L. T. Weng, G. Vereecke, M. J. Genet, P. Bertrand, and W. E. E. Stone. Quantitative xps. part i. experimental determination of the relative analyser transmission function of two different spectrometers - a critical assessment of various methods, parameters involved and errors introduced. *Surface and Interface Analysis*, 20(3):179–192, 1993.

[18] L. T. Weng, G. Vereecke, M. J. Genet, P. G. Rouxhet, J. H. Stone-Masui, P. Bertrand, and W. E. E. Stone. Quantitative xps. part ii. comparison between different quantitative approaches for two different spectrometers - determination of the contamination-reduced thickness, application of the determined transmission functions and accuracy achieved. *Surface and Interface Analysis*, 20(3):193–205, 1993.

[19] P. Ruffieux, P. Schwaller, O. Groning, L. Schlapbach, P. Groning, Q. C. Herd, D. Funnemann, and J. Westermann. Experimental determination of the transmission factor for the omicron ea125 electron analyzer. *Review of Scientific Instruments*, 71(10):3634, 2000/10/.

[20] Y. M. Cross and J. E. Castle. The relationship between transmission efficiencies in the frr and fat modes of an electron spectrometer. *Journal of Electron Spectroscopy and Related Phenomena*, 22(1):53–60, 02 1981.

[21] Carol S. Hemminger, Terry A. Land, Alex Christie, and John C. Hemminger. Empirical electron spectrometer transmission function for applications in quantitative xps. *Surface and Interface Analysis*, 15(5):323–327, 1990.

[22] Sebastian Leung. Visualization of Reciprocal Lattice Structures Using RHEED Data, 2007.

[23] K. Ploog. Microscopical Structuring of Solids by Molecular Beam EpitaxySpatially Resolved Materials Synthesis. *Angewandte Chemie International Edition in English*, 27(5):593–621, 1988.

[24] C. D. Wagner, L. E. Davis, M. V. Zeller, J. A. Taylor, R. H. Raymond, and L. H. Gale. Empirical atomic sensitivity factors for quantitative analysis by electron spectroscopy for chemical analysis. *Surface and Interface Analysis*, 3(5):211–25, 10 1981.

[25] M. P. Seah and G. C. Smith. Aes. accurate intensity calibration of electron spectrometers. results of a bcr interlaboratory comparison co-sponsored by the vamas sca twp. *Surface and Interface Analysis*, 17(12):855–874, 1991.

[26] M. P. Seah. Xps reference procedure for the accurate intensity calibration of electron spectrometers - results of a bcr intercomparison co-sponsored by the vamas sca twa. *Surface and Interface Analysis*, 20(3):243–266, 1993.

[27] Nicholas J.C. Ingle. *Molecular Beam Epitaxial Growth of Complex Novel Oxides*. PhD thesis, Stanford Universtiy, 2001.

[28] J. Ghijsen, LH Tjeng, J. van Elp, H. Eskes, J. Westerink, GA Sawatzky, and MT Czyzyk. Electronic structure of Cu_2O and CuO. *Physical Review B*, 38(16):11322–11330, 1988.

[29] A. Brazdeikis and A. S. Flodstrom. Surface morphology and nucleation of infinite-layer $(Sr, Ca)CuO_2$ films on atomically flat $SrTiO_3$ (100) substrates studied by atomic force microscopy. *Applied Surface Science*, 107:95–101, 1996.

[30] S. Gonda, H. Nagata, M. Kawasaki, M. Yoshimoto, and H. Koinuma. In situ surface analysis of $SrCuO_2$ heteroepitaxy on $SrTiO_3$ substrate using X-ray photoelectron spectroscopy. *Physica C: Superconductivity*, 216(1):160–164, 1993.

[31] LAA Pettersson and PG Snyder. Preparation and characterization of oxidized silver thin films. *Thin Solid Films*, 270(1-2):69–72, 1995.

[32] V. Matijasevic. Atomic oxygen detection by a silver-coated quartz deposition monitor. *Review of Scientific Instruments*, 61(6):1747, 1990.

Appendix A

Intensity Calibration Programs

All of the following scripts were written for Interpretive Data Language (IDL) version 6.3.

A.1 Calibration Script

This script finds the column vector **A**, as per the algorithm described in section 2.2.1. It presupposes the existence of arrays of XPS intensity data named for the X-ray power used in Watts (scan400, scan350, scan300, scan250, scan200, scan150, scan100).

```
p = 6

B = [ -scan400/400.0+scan100/100.0,-scan350/350.0 +
      scan100/100.0, -scan300/300.0+scan100/100.0,
      -scan250/250.0+scan100/100.0, -scan200/200.0
      +scan100/100.0, -scan150/150.0+scan100/100.0]

C = DBLarr( size (B, /dimensions), p)

FOR i = 2, p+1 DO C[*, i-2] = [ double(scan400)^(i)/400.0-
    double(scan100)^(i)/100.0, double(scan350)^(i)/350.0 -
    double(scan100)^(i)/100.0, double(scan300)^(i)/300.0-
    double(scan100)^(i)/100.0, double(scan250)^(i)/250.0-
    double(scan100)^(i)/100.0 , double(scan200)^(i)/200.0-
    double(scan100)^(i)/100.0, double(scan150)^(i)/150.0-
    double(scan100)^(i)/100.0]

A = Invert(Matrix_Multiply(double(C),double( C),
    /Atranspose)) # Matrix_Multiply(double(C),
    double(B), /ATranspose)
```

```
Print , A
```

A.2   Data Correction

This function accepts the data to be corrected and the column vector **A** as
its inputs, and returns the corrected spectrum.

```
function makegood, scan, A
   fixed = dblarr(size(scan, /dimensions))
   temp = size(A, /dimensions)
   fixed = scan
   for i = 2, temp[0]+1 DO fixed += double( A[i-2]*scan^(i))
   return, fixed
END
```